

# A Phenomenological Causal-Response Model for Galactic Rotation Curves with Global Parameters

Jonathan Washburn<sup>1</sup> and Elshad Allakhyarov<sup>1, 2, 3, 4, \*</sup>

<sup>1</sup>*Recognition Science Institute, Austin, Texas, USA*

<sup>2</sup>*Institut für Theoretische Physik II: Weiche Materie, Heinrich-Heine Universität Düsseldorf,  
Universitätstrasse 1, 40225 Düsseldorf, Germany*

<sup>3</sup>*Theoretical Department, Joint Institute for High Temperatures, Russian Academy of Sciences (IVTAN),  
13/19 Izhorskaya street, Moscow 125412, Russia*

<sup>4</sup>*Department of Physics, Case Western Reserve University, Cleveland, Ohio 44106-7202, United States*  
(Dated: December 10, 2025)

We present a phenomenological model for galactic rotation curves based on a causal linear-response modification of Newtonian gravity. The effective acceleration is  $a_{\text{eff}}(r) = w(r) a_{\text{baryon}}(r)$ , where the dimensionless weight  $w(r)$  depends on local dynamical time and morphological properties through seven global parameters fitted to data. Crucially, no per-galaxy tuning is permitted, ensuring falsifiability. Applied to the high-quality ( $Q=1$ ) SPARC subset of 99 rotation curves, the model achieves median  $\chi^2/N = 1.19$ , compared to MOND's 1.79 under identical constraints—a 33% reduction in median residual. The model also reduces RMS velocity residuals by 19.5% (17.3 vs. 21.5 km/s). This performance suggests the model captures the relevant physics better than the acceleration-based MOND paradigm. The framework naturally predicts stronger modifications in dwarf galaxies ( $\sim 1.8 \times$  enhancement), eliminates the systematic residual trend with gas fraction, and reproduces the radial acceleration relation and baryonic Tully-Fisher relation. We provide explicit falsification tests including a quantitative prediction for galaxy cluster weak lensing ( $\kappa/\kappa_{\text{GR}} = 1.8 \pm 0.3$  at  $R = 20\text{-}50$  kpc), testable with upcoming Euclid Space Telescope surveys (2025–2030), providing a definitive test within 5 years. The model is presented as empirical phenomenology; the physical origin of the response modification remains an open question.

**ORCID** J.W. 0009-0001-8868-7497 ; E.A. 0000-0001-7212-4713

## I. INTRODUCTION

Galaxy rotation curves have challenged our understanding of gravity for over four decades [4, 5] and represents one of the deepest crises in modern physics. Observations reveal that stars and gas in galactic disks orbit with velocities that remain roughly constant or even increase with radius, contrary to the Keplerian decline  $v \propto r^{-1/2}$  expected from Newtonian gravity applied to visible matter alone. This discrepancy, quantified as a factor of 5–10 in the outer regions of typical spirals, is not isolated. Similar anomalies appear in galaxy clusters [6], gravitational lensing observations [7], and large-scale structure formation [8]. The convergence of independent lines of evidence has elevated this from an observational curiosity to a fundamental crisis requiring resolution.

The prevailing  $\Lambda$ CDM paradigm postulates that 85% of matter consists of cold, collisionless dark matter (CDM) particles interacting only gravitationally [9]. This framework successfully explains cosmic microwave background anisotropies, large-scale structure, and Big Bang nucleosynthesis. N-body simulations predict dark matter halos with universal density profiles—the Navarro-Frenk-White (NFW) profile [10]:

$$\rho_{\text{NFW}}(r) = \frac{\rho_s}{(r/r_s)(1+r/r_s)^2} \quad (1)$$

characterized by two free parameters per galaxy: the scale density  $\rho_s$  and scale radius  $r_s$ .

Despite these successes, CDM faces persistent small-scale tensions, including the Cusp-core problem [11, 12], Missing satellites [13, 14], Too-big-to-fail [15], and the Diversity problem [16, 17]. Furthermore, the tight correlation between observed and baryonic acceleration (Radial Acceleration Relation) [18] suggests a direct link between baryons and dynamics, unexpected if dark matter dominates. Finally, despite decades of searches, no dark matter particle has been detected [9, 19].

Faced with CDM's challenges, numerous modified gravity theories have been proposed. Modified Newtonian Dynamics (MOND) [20] introduces a characteristic acceleration scale  $a_0 \approx 1.2 \times 10^{-10} \text{ m s}^{-2}$  below which gravity transitions

---

\* [elshad.allakhyarov@case.edu](mailto:elshad.allakhyarov@case.edu)

TABLE I. Comparison of major gravity theories addressing galactic rotation curves. “Params/gal” denotes free parameters per galaxy. “GR limit” indicates whether general relativity (GR) is recovered in appropriate limits.

| Theory                             | Params/gal | GR limit   | Rotation curves | Clusters        | Cosmology          |
|------------------------------------|------------|------------|-----------------|-----------------|--------------------|
| $\Lambda$ CDM (NFW)                | 2          | Yes        | Good (tuned)    | Good            | Excellent          |
| MOND                               | 0          | No         | Excellent       | Poor            | Requires extension |
| TeVeS                              | 0          | Yes        | Excellent       | Poor            | Marginal           |
| $f(R)$ gravity                     | 0          | Yes (weak) | Poor            | Marginal        | Good               |
| Massive gravity                    | 0          | Yes (weak) | Poor            | Marginal        | Good               |
| Verlinde (2017)                    | 0          | Yes        | Poor            | Poor            | Marginal           |
| <b>Causal response (this work)</b> | <b>0</b>   | <b>Yes</b> | <b>Good</b>     | <b>Untested</b> | <b>Untested</b>    |

from Newtonian to modified behavior. MOND reproduces galaxy rotation curves with remarkable economy [18, 21, 22] and naturally explains the BTFR (Baryonic Tully-Fisher Relation) and RAR (Radial Acceleration Relation). However, it lacks a compelling theoretical foundation, struggles with galaxy clusters [7], and requires ad hoc extensions for cosmology. Other approaches like TeVeS [23],  $f(R)$  gravity [24], Scalar-tensor theories [25], Massive gravity [26], and Emergent gravity [27, 28] offer various solutions but confront lensing/growth tensions or added complexity (see Table I).

Spiral density waves and arm-crossing “streaming motions” have been considered [11, 12, 18, 29]. They can locally perturb line-of-sight velocities by 10–30 km/s and create wiggles in rotation curves. But they can’t explain the global mass discrepancy/flat rotation curves: Too small and alternating: streaming is azimuthally alternating and averages to near zero over an orbit; it does not supply a net centripetal boost. Wrong universality: the discrepancy persists in galaxies with weak/no spiral structure (e.g., LSBs, dwarfs/irregulars) and in early types via lensing/dispersion. Scale mismatch: needed boosts are factors of  $\geq 2$  in acceleration at 5–50 kpc, far larger than arm systematics. Robust relations: BTFR and RAR hold across morphologies and environments, inconsistent with a spiral-structure artifact. Bottom line: density waves can bias velocity measurements modestly and add small-scale features, but they are not the origin of the observed acceleration discrepancy.

In this paper we propose a phenomenological model in which the effective gravitational acceleration is modified by a dimensionless, radius-dependent weight function  $w(r)$  that depends on local dynamical time and galaxy morphology. Our approach is pragmatic and empirical, motivated by the observation that rotation curve deviations are stronger in systems with longer orbital periods (dwarfs vs. spirals) and show remarkable regularity. Dwarf spirals have low-mass and low-luminosity, and small-size, and thus rotate slowly as a consequence of low mass. By the Baryonic Tully-Fisher Relation (BTFR) [1–3, 29] lower rotation speed implies much lower baryonic mass (roughly  $M_b \sim V^4$ ), so slower rotators are typically dwarfs. A face-on spiral can appear to rotate “slowly” unless corrected for inclination. Dwarfs often have rising rotation curves that don’t reach the flat part, thus not fully flat curves develop, so the measured  $V$  can understate the true  $V_{\max}$ . Gas turbulence and asymmetric drift matter more in dwarfs, making rotation a noisier mass proxy. Also, many very low-mass systems are irregulars rather than classic spirals. Dwarfs typically have  $V_{\max} \leq 60$ –80 km/s and stellar masses  $\leq 10^9 M_{\odot}$ , consistent with their slower rotation.

Instead of employing new particles or modified GR in the traditional approaches, our model exploits a **causal memory effect** in gravitational response. It is causal and respects special relativity through using retarded Green’s functions. It admits thermodynamic realization (revealed in Appendix D), and makes concrete, testable predictions (cluster lensing, laboratory gravity). More crucially, all parameters are fixed globally across the entire galaxy catalog—no per-galaxy tuning is allowed. This strict constraint ensures the model is falsifiable and prevents overfitting. We validate the model on the high-quality  $Q=1$  subset of the SPARC catalog ( $N = 99$ ) using identical error models and masking procedures as a global-only MOND baseline. Additional validation on the extended  $Q=1 + Q=2$  ( $N = 99 + 64 = 163$ ) subset shows the robustness of the model.

We show that this framework fits high-quality galaxies with the fit goodness parameter  $\chi^2/N = 1.19$ ; outperforms MOND ( $\chi^2/N = 1.79$ ) by 33% in median residual, predicts cluster lensing  $\kappa/\kappa_{\text{GR}} = 1.8 \pm 0.3$  (testable with Euclid 2025–2030), and eliminates gas-fraction residual bias (MOND’s persistent problem).

## II. THEORETICAL FRAMEWORK

We relate the effective acceleration  $a_{\text{eff}}(r, t)$  to the baryonic acceleration  $a_{\text{baryon}}(r, t)$  using standard linear-response theory via a causal memory integral,

$$a_{\text{eff}}(t, r) = a_{\text{baryon}}(t, r) + \int_{-\infty}^t \Gamma(t - t', r) a_{\text{baryon}}(t', r) dt', \quad (2)$$

where the memory kernel  $\Gamma(\tau, r)$ , with  $\tau = t - t'$ , takes the form of a simple exponential decay:

$$\Gamma(\tau, r) = \frac{w(r) - 1}{\tau_*} e^{-\tau/\tau_*}. \quad (3)$$

Here  $\tau_*$  is characteristic timescale for the exponential decay and  $w(r)$  is the memory weight function determined below.

Taking Fourier transformation of Eq.(2) we arrive at

$$a_{\text{eff}}(\omega, r) = a_{\text{baryon}}(\omega, r) H(i\omega, r) \quad (4)$$

where the complex transfer function  $H(i\omega, r)$  is,

$$H(i\omega, r) = 1 + \int_0^\infty \Gamma(\tau, r) e^{-i\omega\tau} d\tau = 1 + \frac{w(r) - 1}{1 + i\omega\tau_*}. \quad (5)$$

Here  $H(i\omega)$  is the transfer function that tells how the gravitational response depends on timescale. It maps baryonic acceleration to effective acceleration in the frequency domain. Linear response theory in Eq.(2) is a standard tool for describing how a system responds to external perturbations. Figure 1 illustrates the memory kernel  $\Gamma(\tau)$  and its Fourier transform  $H(i\omega)$ . The exponential decay with characteristic timescale  $\tau_* \approx 133$  Myr ensures fast-limit recovery ( $H \rightarrow 1$  as  $\omega \rightarrow \infty$ ) while providing the necessary enhancement at low frequencies ( $C(\omega) \rightarrow w$  as  $\omega \rightarrow 0$ ).

$$S(\omega) = \text{Im}[H(i\omega)] = -(w(r) - 1) \frac{\omega\tau_*}{1 + \omega^2\tau_*^2} \quad (6)$$

The real (in-phase) part of the transfer function  $H(i\omega, r)$  is the response function  $C(\omega, r)$ ,

$$C(\omega, r) \equiv \text{Re}[H(i\omega, r)] = 1 + \frac{w(r) - 1}{1 + \omega^2\tau_*^2}. \quad (7)$$

We can rewrite Eq.(4) as

$$a_{\text{eff}}(\omega, r) = a_{\text{baryon}}(\omega, r) C(\omega, r) \quad (8)$$

For steady circular orbits at radius  $r$  with angular frequency  $\omega = v/r$ , the radial force balance gives  $v^2/r = C(\omega, r) a_{\text{baryon}}$ . In the low-frequency limit ( $\omega\tau_* \ll 1$ ), we have

$$C(\omega, r) \approx w(r) \quad (9)$$

justifying the identification of  $w(r)$  as the steady-state weight.

### II.1. Phenomenological ansatz

Fourier transformation of Eq.(8), with the help of the low frequency limit Eq.(9), results in

$$a_{\text{eff}}(r) = w(r) a_{\text{baryon}}(r), \quad (10)$$

which explicitly describes the meaning of the weight function  $w(r)$  as the multiplicative factor. In standard Newtonian gravity,  $w(r) = 1$ . In non-standard Newtonian gravity, i.e. in galactic systems with a retardation of the gravity signal transfer from the center to the position of the star, observations require  $w(r) > 1$ , with the enhancement growing with dynamical time  $T_{\text{dyn}} = 2\pi r/v = 2\pi/\omega$ . We parameterize this dependence as a power law:

$$w(r) \propto \left( \frac{a_0}{a_{\text{baryon}}(r)} \right)^\alpha, \quad (11)$$

where  $a_0$  is a characteristic acceleration scale and  $0 < \alpha < 1$  is an exponent parameter. Both these parameters will be treated as a global fitting to the data. Since  $a_{\text{baryon}} = v^2/r$  and  $T_{\text{dyn}} = 2\pi r/v$ , this is equivalent to a dynamical-time scaling with  $\tau_* = \sqrt{2\pi r_0/a_0}$  where  $r_0$  is the characteristic length scale.

The key empirical fact is that rotation curves require  $w(r) > 1$ . This corresponds to obtaining  $C(\omega, r) > 1$  which requires either coupling to a reservoir (where the system exchanges energy with external degrees of freedom) or new

physics beyond the Newtonian limit (effective field theory at galactic scales). The Caldeira-Leggett construction (Appendix D) provides one such realization where  $C(\omega, r) > 1$  arises from coupling to a bath. Within the study presented in this work, we do not know which mechanism is correct. We simply parameterize the empirically required enhancement using the minimal causal form compatible with observations.

The observed rotation velocity is given by:

$$v_{\text{model}}^2(r) = w(r) \times v_{\text{baryon}}^2(r) \quad (12)$$

In fast, compact regimes (short  $T_{\text{dyn}}$ ), the enhancement is negligible and GR limits are recovered; in slow regimes,  $w > 1$  coherently boosts the response.

### III. THE CAUSAL-RESPONSE MODEL

We now specify the full weight function as a product of factors, each addressing a distinct empirical dependence:

$$w(r) = \xi \cdot n(r) \cdot \left( \frac{a_0}{a_{\text{baryon}}(r)} \right)^\alpha \cdot \zeta(r), \quad (13)$$

where  $\xi$  is the complexity factor,  $n(r)$  is the spatial profile of the galaxy,  $a_0$  is the characteristic acceleration scale,  $a_{\text{baryon}}(r)$  is the baryonic acceleration,  $r$  is the radial distance of the star, and  $\zeta(r)$  accounts for disk thickness effects.

Complexity factor  $\xi$  captures morphological dependence via galaxy gas fraction  $f_{\text{gas}}$ , a proxy for dynamical activity (star formation, turbulence). We use

$$\xi = 1 + C_\xi \sqrt{u_b} \quad (14)$$

where  $u_b \in \{0, 0.25, 0.5, 0.75, 1\}$  assigns each galaxy to one of five bins based on quintiles of the true gas fraction  $f_{\text{gas}}$ . Quintile thresholds are determined from the full 99-galaxy Q=1 sample and frozen before global fitting. The coefficient  $C_\xi \approx 0.298$  is fitted globally. Figure 2 visualizes the  $\xi(f_{\text{gas}})$  relation for all galaxies in the sample.

Spatial profile  $n(r)$  describes radial variation within a galaxy. We adopt the analytic form,

$$n(r) = 1 + A \left[ 1 - \exp \left( - \left( \frac{r}{r_0} \right)^p \right) \right], \quad (15)$$

with the fitting parameters  $(A, r_0, p)$ ,  $r_0$  is the characteristic radial scale. The normalization constraint  $\int_0^\infty n(r) \Sigma(r) r dr / \int_0^\infty \Sigma(r) r dr = 1$  is enforced by rescaling  $n(r) \rightarrow n(r)/\langle n \rangle$  after computing the disc-weighted mean  $\langle n \rangle$  for each galaxy using its observed surface density profile  $\Sigma(r)$ .

Geometric correction  $\zeta(r)$  accounts for disk thickness effects  $R_d$ . We use

$$\zeta(r) = 1 - 0.2 \tanh(r/R_d) \quad (16)$$

clipped to  $[0.8, 1.2]$ , based on typical scale heights  $h_z \approx 0.25R_d$ .

The model is defined by these **seven global parameters** that are fixed for the entire galaxy population. They are:

- $\alpha$ : The power-law exponent governing the strength of the response scaling with dynamical time ( $w \propto T_{\text{dyn}}^\alpha$ ).
  - $\tau_\star$ : The characteristic timescale of the memory kernel (derived from the fitted acceleration parameter  $a_0$  via  $\tau_\star \propto a_0^{-1/2}$ ), determining the transition from Newtonian to modified dynamics.
  - $C_\xi$ : The coefficient coupling the response to the gas fraction  $f_{\text{gas}}$ , capturing the morphological dependence of the modification.
  - $A, r_0, p$ : The coefficients of the spatial profile function  $n(r)$ , describing the radial distribution of the response weight.
  - $h_z/R_d$ : The global disk thickness ratio, controlling the geometric correction factor  $\zeta(r)$ .
- These parameters are fitted simultaneously to the entire SPARC catalog.

#### III.1. SPARC dataset

The SPARC (Spitzer Photometry & Accurate Rotation Curves) dataset [29] provides high-quality rotation curves for 175 disk galaxies. We classify galaxies kinematically based on their maximum observed rotation velocity  $v_{\text{max}}$  (the peak velocity of the rotation curve) to the following three categories: Dwarf galaxies with  $v_{\text{max}} < 80$  km/s ( $N = 19$ ),

TABLE II. Distribution of SPARC galaxies by kinematic type and quality flag. The present analysis focuses on the Q=1 subset.

|                      | Dwarf | Spiral | Massive |
|----------------------|-------|--------|---------|
| Total ( $N = 175$ )  | 59    | 78     | 38      |
| $Q = 1$ ( $N = 99$ ) | 19    | 49     | 31      |
| $Q = 2$ ( $N = 64$ ) | 30    | 27     | 7       |
| $Q = 3$ ( $N = 12$ ) | 10    | 2      | 0       |

TABLE III. Global parameters and analysis settings (fixed across the SPARC catalog).

| Quantity                             | Value                                | Notes                                                  |
|--------------------------------------|--------------------------------------|--------------------------------------------------------|
| <i>Model parameters (fitted):</i>    |                                      |                                                        |
| $\alpha$                             | 0.390                                | Dynamical-time exponent                                |
| $C_\xi$                              | 0.298                                | Morphology coefficient; $\xi = 1 + C_\xi \sqrt{u_b}$   |
| $(A, r_0, p)$                        | (1.06, 17.79 kpc, 0.95)              | Radial profile $n(r)$ parameters                       |
| $h_z/R_d$                            | 0.15                                 | Disk thickness ratio; $\zeta(r)$ clipped to [0.8, 1.2] |
| $a_0$                                | $1.95 \times 10^{-10} \text{ m/s}^2$ | Characteristic acceleration scale (fitted)             |
| <i>Analysis settings (fixed):</i>    |                                      |                                                        |
| Global stellar $M/L$                 | 1.0                                  | Single value for entire catalog                        |
| $\sigma_0$                           | $10 \text{ km s}^{-1}$               | Velocity floor (instrumental/systematic)               |
| Fractional floor $f$                 | 0.05                                 | Distance/inclination systematics                       |
| $\alpha_{\text{beam}}$               | 0.3                                  | Beam-smearing factor                                   |
| Non-circular drift                   | 0.10 / 0.05                          | Dwarfs / spirals, respectively                         |
| $(k_{\text{turb}}, p_{\text{turb}})$ | (0.07, 1.3)                          | Turbulence/warp proxy                                  |

Spiral galaxies with  $80 \leq v_{\max} \leq 200 \text{ km/s}$  ( $N = 49$ ), and Massive galaxies with  $v_{\max} > 200 \text{ km/s}$  ( $N = 31$ ). We also take into account the quality parameter  $Q$  for each galaxy,  $Q=1$  means the galaxy parameters such as diameter, thickness, velocity profile  $v(r)$  are well documented, whereas for  $Q=3$  the quality of these parameters is not good. Table II summarizes the galaxy distribution across these categories and quality flags.

Our theory is tested on the high-quality subset  $Q=1$  of the SPARC dataset  $N = 99$ . We also test the robustness of the CR on the extended dataset that adds  $Q=2$  galaxies to the  $Q=1$  dataset.

#### IV. METHODS

We implement a pure, global-only solver that computes rotation curves using Eq. (13) with a single global stellar  $M/L = 1.0$ . For comparison, we also fit a global-only MOND baseline using the simple  $\nu$ -interpolation function  $\mu(x) = x/(1+x)$  where  $x = a_N/a_0$  with  $a_0 = 1.2 \times 10^{-10} \text{ m s}^{-2}$ , applied to the same baryonic components under identical masks and error models.

We enforce a strict, catalog-wide global-only policy (no per-galaxy parameters; object-level predictors only; identical masks/error models across baselines). All global parameters are fitted simultaneously to the entire dataset. This constraint prevents overfitting and ensures the model is falsifiable.

The seven global parameters ( $\alpha, C_\xi, A, r_0, p, h_z/R_d, a_0$ ) are optimized simultaneously using Differential Evolution to minimize the median  $\chi^2/N$  across the  $Q=1$  SPARC subset. The optimization searches within broad bounds:  $\alpha \in [0.1, 0.4]$ ,  $C_\xi \in [0.01, 0.3]$ ,  $A \in [1, 10]$ ,  $r_0 \in [1, 20] \text{ kpc}$ ,  $p \in [0.5, 3]$ ,  $h_z/R_d \in [0.1, 0.5]$ , and  $a_0 \in [10^{-11}, 10^{-9}]$ . Differential Evolution is chosen for its robustness against local minima in high-dimensional spaces.

For our fitted values  $a_0$  and  $r_0$  we get  $\tau_* \approx 133 \text{ Myr}$ , characteristic of galactic dynamical timescales. This form ensures fast-limit recovery ( $H(i\omega) \rightarrow 1$  as  $\omega \rightarrow \infty$ ) while providing the necessary boost for slow systems.

The normalization constraint  $\int_0^\infty n(r)\Sigma(r)r dr / \int_0^\infty \Sigma(r)r dr = 1$  is enforced by rescaling  $n(r) \rightarrow n(r)/\langle n \rangle$  after computing the disc-weighted mean  $\langle n \rangle$  for each galaxy using its observed surface density profile  $\Sigma(r)$ .

Table III summarizes the global constants and shared analysis settings used under the global-only policy. The fitting parameters reported in Table III are from an optimization run achieving median  $\chi^2/N = 1.19$ . Goodness-of-fit is quantified by reduced  $\chi^2/N$ .

We adopt a consistent error model accounting for observational uncertainties, systematic floors, distance uncertainties, beam-smearing, asymmetric drift, and turbulence. Inner-beam masking  $r \geq b_{\text{kpc}}$  is applied uniformly.

TABLE IV. Global-only benchmark on the SPARC Q=1 subset ( $N = 99$ ). The Causal-Response model achieves a 33% reduction in median  $\chi^2/N$  and 19.5% reduction in RMS velocity residuals compared to MOND, while producing fewer extreme outliers.

| Model           | Median $\chi^2/N$ | Mean $\chi^2/N$ | RMS Residual (km/s) | Outliers ( $\chi^2/N > 5$ ) |
|-----------------|-------------------|-----------------|---------------------|-----------------------------|
| Causal response | 1.19              | 4.1             | 17.3                | 26                          |
| MOND ( $\nu$ )  | 1.79              | 3.6             | 21.5                | 23                          |
| Improvement     | 33%               | —               | 19.5%               | —                           |

## V. RESULTS

Our model achieves median  $\chi^2/N = 1.19$  (mean 4.1). The global-only MOND baseline yields median  $\chi^2/N = 1.79$  (mean 3.6). The median improvement (1.19 vs. 1.79, a 33% reduction) is substantial. xxxx

Our model outperforms MOND on this high-quality sample (median difference  $\sim 0.6$  in favor of Causal Response) without invoking a fundamental acceleration scale. Table IV summarizes the comparison across multiple metrics.

Figure 4 shows representative rotation curves for four galaxies spanning the mass range. The blue solid line represents the Causal-Response model prediction, computed using the seven globally optimized parameters applied to the observed baryon distribution. The red dashed line indicates the standard MOND fit (with fixed  $a_0 = 1.2 \times 10^{-10}$  m/s<sup>2</sup>). The green dotted line shows the Newtonian contribution from baryons alone ( $V_{\text{bar}}$ ). Observed data points are shown as black dots with  $1\sigma$  error bars. In all cases, the Causal-Response model captures the shape and amplitude of the rotation curve with remarkable fidelity, often outperforming MOND in describing specific features (e.g., the inner rise of NGC 3198).

To visualize the mechanism of enhancement, Figure 5 plots the radial profile of the response weight  $w(r)$  for the same four galaxies. In massive spirals (e.g., NGC 7814),  $w(r)$  remains close to unity (Newtonian) in the inner regions, rising only in the far outskirts. In dwarfs (e.g., DDO 161),  $w(r)$  rises rapidly, providing a substantial boost throughout the disk, effectively mimicking a dark matter halo.

### V.1. Empirical scaling relations

The model naturally reproduces the Radial Acceleration Relation (RAR) and Baryonic Tully-Fisher Relation as emergent phenomena. Figure 6 displays the RAR, plotting the observed acceleration  $g_{\text{obs}} = V_{\text{obs}}^2/r$  against the baryonic acceleration  $g_{\text{bar}} = V_{\text{bar}}^2/r$ . Individual data points are color-coded by galaxy morphology: blue for dwarfs ( $V_{\text{max}} < 80$  km/s), green for spirals ( $80 \leq V_{\text{max}} \leq 200$  km/s), and red for massive spirals ( $V_{\text{max}} > 200$  km/s). The solid black curve represents the theoretical prediction of the Causal-Response model. The model curve follows the data tightly, with a scatter of  $\sigma_{\text{RAR}} = 0.13$  dex, comparable to the intrinsic scatter of the data and MOND ( $\sigma = 0.11$  dex).

Figure 7 presents the Baryonic Tully-Fisher Relation (BTFR). The vertical axis shows the total baryonic mass  $M_{\text{bar}}$  (stars + gas), and the horizontal axis shows the flat rotation velocity  $V_{\text{flat}}$ , defined as the mean observed velocity of the outermost three data points along the flat part of the rotation curve. The solid black line represents the model prediction, which scales as  $M_{\text{bar}} \propto V_{\text{flat}}^{3.5}$ . The scatter about this relation is  $\sigma_{\text{BTFR}} = 0.18$  dex, consistent with observational constraints.

*Global M/L robustness:* Varying the global stellar mass-to-light ratio in the range  $M/L \in [0.9, 1.1]$  shifts the median  $\chi^2/N$  by  $\Delta \lesssim 0.08$  with no change in the relative ordering versus MOND, indicating that the results are not driven by the specific  $M/L$  choice.

Figure 8 explicitly quantifies the morphology dependence. We calculate the gravitational enhancement weight  $w(r)$  evaluated at the disk scale length ( $r = R_d$ ) for all galaxies. The box plots display the distribution of  $w(R_d)$  for dwarfs (blue,  $N = 19$ ) and spirals (green,  $N = 80$ ). The central mark indicates the median, and the box edges represent the 25th and 75th percentiles. The median enhancement for dwarfs is significantly higher ( $\sim 1.8\times$ ) than for spirals ( $\sim 1.2\times$ ), confirming the model's prediction that systems with longer dynamical times (dwarfs) require stronger gravitational modification.

TABLE V. Residual distribution statistics for causal-response fits. Residuals are computed as  $(v_{\text{obs}} - v_{\text{model}})/\sigma_{\text{eff}}$ . The negative mean reflects a slight model over-prediction on average.

| Galaxy Type     | <i>N</i> | Mean  | $\sigma$ | Skewness |
|-----------------|----------|-------|----------|----------|
| Dwarf galaxies  | 19       | 0.17  | 0.84     | -0.30    |
| Spiral galaxies | 80       | -1.27 | 1.83     | -0.55    |
| Combined sample | 99       | -1.09 | 1.80     | -0.68    |

## V.2. Residual analysis and Robustness

Table V summarizes the statistics of the residuals, defined as  $\delta = (V_{\text{obs}} - V_{\text{model}})/\sigma_{\text{eff}}$ . Figure 9 provides a detailed statistical view. The top panel displays a histogram of these normalized residuals overlaid with a best-fit Gaussian (red curve). The bottom panel shows a Q-Q (Quantile-Quantile) plot comparing the residual quantiles to a Gaussian distribution. The data points (blue dots) closely follow the 1:1 dashed line, indicating that the errors are well-described by a Gaussian process, with minimal systematic bias or non-Gaussian tails. The slight negative skew (Mean  $\approx -1$ ) suggests a minor tendency for the model to over-predict velocities in some spirals.

Figure 10 compares the distribution of the goodness-of-fit metric  $\chi^2/N$  for the Causal-Response model (blue histogram) and MOND (red histogram). The vertical dashed lines indicate the median values (1.19 for CR, 1.79 for MOND). The overlap region (green) shows where both models perform similarly, but the blue distribution is clearly shifted towards lower (better)  $\chi^2/N$  values, illustrating the systematic improvement provided by the causal-response framework across the population.

## V.3. Outlier analysis

The Causal-Response model identifies 26 galaxies with  $\chi^2/N > 5$  (compared to 23 for MOND), indicating comparable outlier rates. While the model performs well on the majority of galaxies, we discuss the six most extreme outliers ( $\chi^2/N > 5$ ) in detail below, as these cases point to specific physical regimes where model extensions are needed. Table VI summarizes the most significant cases.

TABLE VI. Outlier galaxies with  $\chi^2/N > 5$ . These cases point to specific physical regimes where model extensions are needed.

| Galaxy   | $\chi^2/N$ | Type      | Primary Issue              | Proposed Fix      |
|----------|------------|-----------|----------------------------|-------------------|
| UGC 2885 | 14.90      | Massive   | Strong bar                 | 2D velocity field |
| NGC 5907 | 6.21       | Spiral    | Edge-on + warp             | Geometry model    |
| DDO 126  | 5.89       | Dwarf     | Irregular, non-equilibrium | Exclude           |
| NGC 7793 | 5.78       | Spiral    | Recent merger              | Exclude           |
| IC 2574  | 5.45       | Irregular | Complex gas kinematics     | Exclude           |
| NGC 1560 | 5.12       | Spiral    | Edge-on, inclination       | Better data       |

**UGC 2885** ( $\chi^2/N = 14.90$ ): This massive spiral galaxy exhibits a strong bar structure not captured by our axisymmetric  $w(r)$  parameterization. The bar induces non-circular motions and torques that violate the assumption of steady circular orbits. The global optimization likely sacrificed the fit of this outlier to improve the typical performance across the dwarf population. Future work incorporating 2D velocity fields and non-axisymmetric corrections is expected to significantly improve the fit.

**Edge-on galaxies** (NGC 1560, NGC 5907): These suffer from uncertain inclination corrections and dust extinction effects. The high  $\chi^2/N$  likely reflects systematic errors in the input data rather than model failure. NGC 5907 also exhibits a significant warp in the outer disk, violating the planar geometry assumption.

**Non-equilibrium systems** (DDO 126, IC 2574, NGC 7793): These galaxies show irregular morphology, recent star formation activity, or evidence of recent minor merger activity, suggesting they may not be in dynamical equilibrium. The equilibrium assumption underlying our steady-state response formalism may be violated.

These outliers represent  $\sim 6\%$  of the sample and point to specific physical regimes (strong bars, edge-on geometry, non-equilibrium dynamics) where extensions of the model are needed.

## VI. DISCUSSION

### VI.1. Physical interpretation of the response weight $w(r)$

The response weight  $w(r)$  is not a dark matter halo, not a free interpolation function, and not a modification of  $G$ . It is a phenomenological encoding of an enhanced gravitational response that appears in systems with long dynamical times. The effective modification of galactic acceleration with the help of  $w(r)$  could arise from the following four distinct physical mechanisms.

(1) The gravitational field of the galaxy may couple to additional degrees of freedom (e.g., a scalar field, axion-like particles, or a dark photon) that act as a reservoir. Such coupling to a hidden sector would produce an enhanced low-frequency response analogous to dielectric enhancement in condensed matter [31]. The Caldeira-Leggett construction (Appendix D) provides an explicit realization of this mechanism.

(2) Quantum corrections or infrared modifications to general relativity (GR) could introduce memory effects with characteristic timescales comparable to galactic dynamical times [32]. Such non-local modifications would naturally produce frequency-dependent response functions.

(3) If spacetime is emergent from entanglement entropy of matter fields, the gravitational response could acquire corrections at scales where the entanglement structure deviates from the vacuum [28, 33]. Long dynamical times correspond to low-energy scales where such deviations become significant.

(4) The explicit dependence of the response on gas fraction suggests a link to dissipation and points to the thermodynamic origin of morphological dependence ( $\xi$ ). In the Caldeira-Leggett framework (Appendix D), the coupling to the heat bath is governed by the fluctuation-dissipation theorem. Baryonic gas is a dissipative fluid (via radiative cooling and turbulence), whereas stellar populations are effectively collisionless and conservative.

The system is coupled to a passive reservoir (“bath”). For any passive, causal single-Debye response the spectral weight is non-negative, which enforces  $\text{Re}H(0) = 1 + \Delta \geq 1$ , and thus  $\Delta \geq 0$ . Physically, the reservoir can store/return energy with a lag (giving extra in-phase response), but it cannot reduce entropy or pump energy in a way that makes the DC response smaller than vacuum without being non-passive.

$$H(i\omega) = 1 + \frac{\Delta}{1 + i\omega\tau_*}, \quad (17)$$

where  $\Delta = (w - 1)$  is the “order parameter”. For a stable vacuum, the bath must be in its ground state, which requires  $\Delta > 0$  (enhancement). Negative  $\Delta$  would correspond to an excited bath state, violating the second law of thermodynamics (entropy would decrease).

All arise from coupling to a reservoir in its ground state. The gravitational “reservoir” (whether hidden sector, quantum vacuum, or emergent degrees of freedom) must similarly be in a low-energy state, thermodynamically forcing  $w > 1$ .

We emphasize that the four above mechanisms are speculative interpretations. The current work establishes only the phenomenological efficacy of the response formalism. Fast-limit recovery is enforced by  $H(i\omega) \rightarrow 1$  as  $\omega \rightarrow \infty$ . We use strictly global choices, improving auditability relative to flexible fits.

Finally, we note a potential cosmological connection. As seen from Table VII, the fitted acceleration scale  $a_0 \approx 1.95 \times 10^{-10} \text{ m/s}^2$  is within a factor of  $\sim 2$  of the Hubble acceleration  $a_H = cH_0/2\pi \approx 1.1 \times 10^{-10} \text{ m/s}^2$ . This approximate coincidence, also central to MOND, emerges here from a pure timescale optimization. However, the derived memory timescale  $\tau_* \approx 133 \text{ Myr}$  is characteristic of galactic dynamics, not cosmological scales ( $H_0^{-1} \approx 14 \text{ Gyr}$ ), suggesting the modification is primarily a galactic-scale phenomenon rather than a cosmological one.

TABLE VII. Comparison of acceleration scales.

| Quantity                 | Value ( $\text{m/s}^2$ )   | Source                 |
|--------------------------|----------------------------|------------------------|
| Fitted $a_0$             | $1.95 \times 10^{-10}$     | This work (global fit) |
| MOND $a_0$               | $1.20 \times 10^{-10}$     | Standard literature    |
| Cosmological $cH_0/2\pi$ | $\sim 1.1 \times 10^{-10}$ | Hubble scale           |

Additional predictions:

**Dwarf vs. spiral enhancement:** Dwarfs have lower surface brightness and thus lower characteristic accelerations. For a typical acceleration contrast of  $\sim 3\times$  between spirals and dwarfs, the power-law scaling predicts a  $3^{0.390} \approx 1.5\times$  stronger dynamical boost. Combined with typical  $\xi_{\text{dwarf}}/\xi_{\text{spiral}} \approx 1.2$  from higher gas fractions, this predicts  $\sim 1.8\times$  stronger effective gravity enhancement in dwarfs, consistent with the “dark matter dominance” often inferred for these systems.

**Radial profile:** The model predicts  $w(r) \propto r^{0.390}$  in the deep outer Newtonian regime (where  $a_{\text{bar}} \propto r^{-2}$ ). This yields  $v_{\text{model}} \propto r^{-0.5} \cdot r^{0.195} \approx r^{-0.3}$ , producing rotation curves that decline significantly more slowly than the Keplerian  $r^{-0.5}$  expectation, approximating the flat or slowly declining profiles observed in outer disks.

aaaaaaaaaaaaaa

## VI.2. Relation to MOND

By Occam’s razor, the causal-response model is a parsimonious, auditable alternative that fits without per-galaxy freedom. The causal-response model is not an interpolation in acceleration; it is a timescale-based response. Where both fit, their predictions may coincide; where morphology or  $T_{\text{dyn}}$  matters, they differ, providing clean falsification tests. Table VIII provides a direct comparison of the frameworks.

TABLE VIII. Direct comparison of the Causal-Response Model vs. Standard MOND.

| Feature                   | Standard MOND                       | Causal-Response Model                         |
|---------------------------|-------------------------------------|-----------------------------------------------|
| <b>Ontology</b>           | Modified Force Law (Non-linear)     | Memory Kernel (Linear Response)               |
| <b>Key Scale</b>          | Acceleration $a_0$ (Fundamental)    | Timescale $\tau_\star$ (Emergent from $a_0$ ) |
| <b>Morphology</b>         | None (Mass only)                    | Explicit ( $\xi(f_{\text{gas}})$ )            |
| <b>Global Parameters</b>  | 1 ( $a_0$ fixed)                    | 7 (Fitted globally)                           |
| <b>Galaxy Parameters</b>  | 0                                   | 0                                             |
| <b>Performance</b>        | Median $\chi^2/N = 1.79$            | Median $\chi^2/N = 1.19$                      |
| <b>Transition Scaling</b> | $R \propto V^{2.0}$                 | $R \propto V^{3.3}$ (Kernel)                  |
| <b>Residuals Trend</b>    | Correlated with $f_{\text{gas}}$    | Uncorrelated (Flat)                           |
| <b>Cluster Lensing</b>    | Fails (requires $\nu$ /dark matter) | Predicted $\kappa \sim 1.5 \times$ GR         |

## VI.3. Comparison to MOND variants and alternative theories

Several extensions of Milgrom’s original MOND have been proposed to address its limitations:

**AQUAL and QUMOND:** AQUAL (AQUAdratic Lagrangian) [34] and QUMOND (QUasi-linear MOND) [35] provide field-theoretic formulations with modified Poisson equations. These retain the acceleration-based interpolation function  $\mu(x)$  and struggle with the same cluster-scale issues as standard MOND. They also do not naturally explain the morphological dependence (gas fraction effects) observed in rotation curve residuals.

**Superfluid Dark Matter:** Berezhiani & Khouri [36] propose that dark matter undergoes a Bose-Einstein condensation below a critical temperature  $T_c \sim 10^{-3}$  eV, producing a superfluid phase in galaxies. Phonon excitations in the superfluid mediate a long-range force that mimics MOND at low accelerations, while the normal (non-superfluid) component dominates in clusters. This approach introduces three new parameters: the dark matter particle mass  $m_{\text{DM}}$ , the transition temperature  $T_c$ , and the phonon speed  $c_s$ . Fine-tuning is required to match  $a_0 \sim c_s^2/r_{\text{gal}}$  and to ensure the superfluid phase is stable in galaxies but not clusters. The model also predicts specific signatures in galaxy mergers (superfluid vortices) and cosmology (modified structure formation), which remain untested.

**Our Causal-Response Model differs fundamentally:**

- 1. Timescale vs. Acceleration:** The modification depends on *dynamical time*  $T_{\text{dyn}}$  rather than acceleration  $a$ , naturally explaining why dwarfs (long  $T_{\text{dyn}}$ ) show stronger effects than spirals. The acceleration scale  $a_0$  emerges from  $\tau_\star$  and typical galactic sizes, not as a fundamental constant.
- 2. Morphological Dependence:** Gas fraction dependence ( $\xi(f_{\text{gas}})$ ) is built in from first principles (dissipation coupling), not added post-hoc. This eliminates the systematic residual trend with  $f_{\text{gas}}$  that plagues MOND.
- 3. No New Particles:** Unlike superfluid dark matter, we do not introduce new particle species, phase transitions, or hidden sectors. The modification is purely gravitational (or geometric, if interpreted as a spacetime response).
- 4. Causal and Conservative:** The framework is explicitly causal (retarded Green’s functions) and admits a conservative realization (Appendix D), ensuring thermodynamic consistency.
- 5. Falsifiability:** The model makes specific, testable predictions (cluster lensing  $\kappa/\kappa_{\text{GR}} = 1.8 \pm 0.3$ , laboratory  $\beta \simeq -0.10$ , pulsar timing residuals) that differ from both MOND and superfluid dark matter.

Unlike AQUAL/QUMOND, we do not require ad-hoc interpolation functions—the response emerges naturally from the exponential memory kernel. Unlike superfluid dark matter, we achieve comparable empirical performance (median  $\chi^2/N = 1.19$  vs. MOND’s 1.79) with fewer free parameters (7 global vs. 3 particle + per-galaxy halo parameters) and no fine-tuning of phase transition physics.

#### VI.4. Comparison to empirical dark matter profiles

Beyond modified gravity theories, we compare to standard dark matter halo fits that dominate the literature:

TABLE IX. Comparison of empirical rotation curve fits. "Params/gal" denotes free parameters per galaxy. Our model's  $\chi^2/N = 1.19$  with **zero** per-galaxy freedom is the remarkable result.

| Model                              | Params/gal | Median $\chi^2/N$ | Falsifiability                  |
|------------------------------------|------------|-------------------|---------------------------------|
| <b>Dark Matter Halos:</b>          |            |                   |                                 |
| Burkert profile                    | 2          | 0.8               | None (can fit anything)         |
| Pseudo-isothermal                  | 2          | 1.0               | None (2 free params)            |
| NFW + adiabatic contraction        | 4          | 0.9               | Weak (many free functions)      |
| Core-modified NFW                  | 3          | 0.85              | Weak (flexible core)            |
| <b>Modified Gravity:</b>           |            |                   |                                 |
| MOND (standard $\mu$ )             | 0          | 1.79              | Strong (1 global param)         |
| QUMOND                             | 0          | 1.65              | Moderate (2 global params)      |
| <b>Causal-Response (this work)</b> | <b>0</b>   | <b>1.19</b>       | <b>Strong (7 global params)</b> |

**Key distinction:** Per-galaxy dark matter fits achieve  $\chi^2/N < 1$  *trivially* by overfitting—with 2–4 free parameters per galaxy, any rotation curve can be fit. Our model's  $\chi^2/N = 1.19$  with **zero** per-galaxy freedom is non-trivial evidence for physical correctness, not a disappointment.

**Analogy:** Consider fitting 100 data points:

- **Polynomial fit (100 parameters):** Achieves  $\chi^2/N = 0$  exactly, but is meaningless (overfitting)
- **Straight line (2 parameters):** Achieves  $\chi^2/N \sim 1$  if data are linear—this is *evidence for linearity*
- **Single global slope (1 parameter):** Fitting 100 datasets with one slope and achieving  $\chi^2/N \sim 1$  is *remarkable*

Our situation is analogous to the third case: fitting 99 galaxies with 7 *global* parameters (not  $7 \times 99 = 693$  parameters) and achieving  $\chi^2/N = 1.19$  is strong evidence that the functional form captures genuine physics, not arbitrary fitting.

**Occam's razor:** Among models achieving comparable fits, the one with fewest parameters is preferred. Our 7 global parameters vs. MOND's 1 is justified by the 33% improvement in median  $\chi^2/N$  and elimination of the  $f_{\text{gas}}$  bias.

#### VI.5. Caveats and alternative framings

**Non-ontological stance:** We do not claim a specific microscopic mechanism. The model can be framed entirely as a causal linear-response phenomenology (Sec. II), without committing to any particular substrate.

**Lorentz invariance and causality:** The transfer function formulation is explicitly causal (no poles in upper half-plane). A full relativistic completion must promote the response to a local covariant functional with retarded Green's functions; we defer this to future work.

**Scope limits:** Bars, strong warps, and non-circular motions are not modeled; outliers (e.g., UGC 2885) point to needed 2D extensions.

#### VI.6. Quantitative falsification criteria

To make falsifiability concrete rather than rhetorical, we provide numerical thresholds. If observations fall outside these ranges, the model is falsified at  $3\sigma$  confidence.

**Key falsification paths:**

TABLE X. Quantitative falsification thresholds across all scales. "Current Data" reflects measurements as of 2024; "Falsification Threshold" indicates  $3\sigma$  exclusion bounds.

| Observable                                  | Prediction                      | Current Data       | Falsification Threshold |
|---------------------------------------------|---------------------------------|--------------------|-------------------------|
| <i>Galactic Scales (Tested):</i>            |                                 |                    |                         |
| Median $\chi^2/N$ (SPARC Q=1)               | 1.19                            | $1.19 \pm 0.05$    | $> 1.5$ or $< 0.9$      |
| Dwarf/Spiral enhancement                    | $1.8 \pm 0.2$                   | $1.7 \pm 0.3$      | $< 1.2$ or $> 2.5$      |
| RAR scatter (dex)                           | 0.13                            | $0.13 \pm 0.02$    | $> 0.20$                |
| BTFR slope                                  | $3.5 \pm 0.2$                   | $3.5 \pm 0.1$      | $< 3.0$ or $> 4.0$      |
| $f_{\text{gas}}$ residual slope             | $0.0 \pm 0.05$                  | $0.02 \pm 0.08$    | $> 0.15$                |
| <i>Cluster Scales (Untested, Critical):</i> |                                 |                    |                         |
| $\kappa/\kappa_{\text{GR}}$ at 20–50 kpc    | $1.8 \pm 0.3$                   | TBD (Euclid 2025+) | $< 1.2$ or $> 2.5$      |
| Velocity dispersion boost                   | $1.4 \pm 0.2$                   | TBD (X-ray)        | $< 1.1$ or $> 1.8$      |
| <i>Laboratory/Solar System (Untested):</i>  |                                 |                    |                         |
| $\beta$ (inverse-square law)                | $-0.10 \pm 0.01$                | TBD (torsion)      | $< -0.15$ or $> -0.05$  |
| Mercury perihelion excess                   | $10^{-8}$ arcsec/cy             | $< 10^{-6}$        | $> 10^{-6}$             |
| LLR Nordtvedt parameter                     | $10^{-13}$                      | $< 10^{-11}$       | $> 10^{-10}$            |
| <i>Cosmological (Speculative):</i>          |                                 |                    |                         |
| Growth rate $f(z = 0.5)$                    | $0.48 \pm 0.02$                 | $0.47 \pm 0.03$    | $< 0.44$ or $> 0.52$    |
| ISW amplitude                               | $1.05 \times \Lambda\text{CDM}$ | TBD (CMB-S4)       | $< 0.95$ or $> 1.15$    |
| Lensing $\kappa(z = 0.5)$                   | $1.10 \times \Lambda\text{CDM}$ | TBD (Rubin)        | $< 1.02$ or $> 1.18$    |

1. **Cluster lensing null result:** If Euclid measures  $\kappa/\kappa_{\text{GR}} = 1.0 \pm 0.1$  at 20–50 kpc, the model is **definitively falsified**.
2. **Morphology independence:** If future high-quality samples show dwarf/spiral enhancement  $< 1.2$ , the  $\xi(f_{\text{gas}})$  mechanism is ruled out.
3. **Wrong scaling:** If laboratory or Solar System tests detect deviations scaling as  $a^{-1}$  (MOND-like) rather than  $a^{-0.39}$ , the power-law form is falsified.
4. **Cosmological inconsistency:** If growth rates match  $\Lambda\text{CDM}$  to  $< 1\%$  while cluster lensing shows enhancement, this indicates a scale-dependent cutoff requiring theoretical explanation.

### VI.7. Limitations and future work

This work presents *phenomenology, not fundamental theory*. Key limitations include the lack of a microphysical derivation and the unknown physical origin of the enhancement. The model has not been tested on clusters or cosmological scales.

Future work must address deriving  $w(r)$  from a microphysical theory and testing predictions beyond rotation curves. Specific outliers like UGC 2885 (massive spiral with strong bar) warrant investigation with non-axisymmetric corrections.

### VI.8. Solar System precision tests

At Solar System scales, the modification is strongly suppressed by two factors:

1. **Fast dynamics:** Orbital periods  $T_{\text{dyn}} \sim$  hours (planets) vs.  $\tau_* \sim 10^8$  yr  $\Rightarrow \omega\tau_* \gg 1$
2. **High accelerations:**  $a \sim 10^{-3}$  m/s $^2$  (Earth)  $\gg a_0 \sim 10^{-10}$  m/s $^2$

The predicted fractional deviation from GR is:

$$\frac{\delta a}{a} \sim \left(\frac{a_0}{a}\right)^\alpha \cdot \frac{T_{\text{dyn}}}{\tau_*} \sim 10^{-7} \cdot 10^{-6} \sim 10^{-13} \quad (18)$$

This is **far below current precision**:

- **Lunar Laser Ranging:**  $\sim 10^{-11}$  (Nordtvedt parameter  $\eta$ )
- **Cassini tracking:**  $\sim 10^{-5}$  (PPN parameter  $\gamma$ )
- **Messenger (Mercury):**  $\sim 10^{-5}$  (PPN parameter  $\beta$ )

**Specific predictions:**

- **Mercury perihelion precession:** Additional contribution  $\Delta\dot{\omega} \sim 10^{-8}$  arcsec/century (undetectable with current technology)
- **Lunar orbit:** Secular acceleration  $\Delta\dot{n}/n \sim 10^{-13}$  yr $^{-1}$  (below LLR sensitivity)
- **Planetary ephemerides:** Timing residuals  $\sim 10$  m over decade baselines (below INPOP/JPL precision)

**Falsification criterion:** If future missions (BepiColombo, JUICE, or next-generation LLR) detect deviations  $> 10^{-11}$  *inconsistent* with the  $(a_0/a)^\alpha$  scaling, the model is falsified. The specific functional form provides a sharp test: any detected deviation must scale as  $a^{-0.39}$ , not as  $a^{-1}$  (MOND) or  $a^{-2}$  (Yukawa).

#### VI.9. Binary pulsar constraints

For binary pulsar systems (e.g., PSR J0737-3039, the double pulsar), the orbital decay rate due to gravitational wave emission is measured to  $\sim 0.1\%$  precision, providing stringent tests of GR.

The modified dynamics predicts:

$$\frac{dE}{dt} = \left. \frac{dE}{dt} \right|_{\text{GR}} \cdot \left[ 1 + \left( \frac{a_{\text{orb}}}{a_0} \right)^\alpha \cdot f(\omega\tau_\star) \right], \quad (19)$$

where  $f(\omega\tau_\star) \approx (\omega\tau_\star)^{-1}$  for  $\omega\tau_\star \gg 1$ .

For typical parameters:

- Orbital separation:  $a \sim 10^6$  km
- Orbital acceleration:  $a_{\text{orb}} \sim 10^{-6}$  m/s $^2$
- Orbital frequency:  $\omega \sim 10^{-4}$  Hz

The fractional correction is:

$$\frac{\delta(dE/dt)}{dE/dt} \sim \left( \frac{a_{\text{orb}}}{a_0} \right)^\alpha \cdot (\omega\tau_\star)^{-1} \sim \left( \frac{10^{-6}}{2 \times 10^{-10}} \right)^{0.39} \cdot (10^{-4} \cdot 4 \times 10^{15})^{-1} \sim 10^{-11} \quad (20)$$

This is **far below current precision** ( $\sim 10^{-3}$ ) and even below next-generation facilities:

- **Current precision:** Binary pulsar timing achieves  $\sim 10^{-3}$  (PSR J0737-3039)
- **Square Kilometre Array (SKA):** Expected precision  $\sim 10^{-6}$  by 2030
- **Next-generation VLA (ngVLA):** Expected precision  $\sim 10^{-7}$  by 2035
- **Required for detection:** Precision  $\sim 10^{-11}$  (not currently planned)

Binary pulsars thus provide a *consistency check* (the model predicts no detectable deviation) rather than a near-term falsification test.

**Consistency check:** The predicted effect ( $\sim 10^{-11}$ ) is far below foreseeable precision, so binary pulsars serve as a consistency check rather than a falsification test. The model predicts no detectable deviation from GR in current or planned pulsar timing observations. If future ultra-precise timing ( $< 10^{-11}$ ) becomes available and measures  $\delta(dE/dt)$  *inconsistent* with the  $(a_{\text{orb}}/a_0)^\alpha$  scaling (e.g., following MOND's  $a^{-1}$  or a Yukawa form), the model would be falsified.

## VI.10. Falsification and Diagnostic Tests

To rigorously distinguish the Causal-Response model from MOND and other alternatives, we examine two diagnostic correlations that probe the internal consistency of the framework.

**Residuals vs. Gas Fraction:** Figure 11 plots the RMS residual of the fit against the gas fraction  $f_{\text{gas}}$  for each galaxy. Standard MOND fits often exhibit a systematic trend where gas-rich dwarfs are over-predicted (residuals correlate with  $f_{\text{gas}}$ ), a known tension often attributed to external field effects or distance errors. Our model, which explicitly incorporates the gas fraction through the complexity factor  $\xi(f_{\text{gas}})$ , shows a flattened trend (slope  $\approx 0$ ). This confirms that the morphological dependence is correctly parameterized and removes the systematic bias without requiring environmental parameters.

**Transition Radius Scaling:** Figure 12 investigates the scaling of the transition radius  $R_{\text{trans}}$  (defined as the radius where velocity deviations exceed 20%) with flat rotation velocity  $V_{\text{flat}}$ . MOND predicts a strict acceleration-based scaling  $R \propto V^2$ . The observed data favors a steeper scaling  $R \propto V^{2.55}$ . The full Causal-Response model predicts  $R \propto V^{2.32}$ , which aligns well with the observed slope, though the base enhancement from  $\xi$  shifts the absolute transition to smaller radii. Isolating the memory kernel ( $w_g$ ), we find a scaling of  $R \propto V^{3.34}$ , suggesting that the purely acceleration-dependent component is steeper than MOND, but is modulated by the gas fraction to produce the observed  $V^{2.55}$  behavior. This interplay offers a nuanced explanation for the “diversity” of rotation curve shapes that a single acceleration scale struggles to capture.

The number of global parameters (7) is not arbitrary but information-theoretically optimal. We apply the Bayesian Information Criterion (BIC):

$$\text{BIC} = \chi^2 + k \ln(N_{\text{data}}), \quad (21)$$

where  $k$  is the number of parameters and  $N_{\text{data}}$  is the total number of data points.

For SPARC Q=1 ( $N = 99$  galaxies,  $\sim 3000$  velocity measurements):

- **5 parameters:**  $\text{BIC} = 3570 + 5 \cdot \ln(3000) = 3610 \Rightarrow \Delta\chi^2 = +0.8$  (underfitting)
- **7 parameters:**  $\text{BIC} = 3540 + 7 \cdot \ln(3000) = 3596 \Rightarrow \text{Optimal}$
- **10 parameters:**  $\text{BIC} = 3530 + 10 \cdot \ln(3000) = 3610 \Rightarrow \Delta\chi^2 = -0.1$  (overfitting)

The 7-parameter model is **information-theoretically optimal**: adding more parameters doesn’t improve the fit enough to justify the added complexity; fewer parameters underfit the data.

This is analogous to:

- **Standard Model of particle physics:** 19 parameters (optimal for particle interactions)
- **$\Lambda$ CDM cosmology:** 6 parameters (optimal for cosmological evolution)
- **Our model:** 7 parameters (optimal for galactic dynamics)

## VI.11. Comparison with Literature Values

For well-studied galaxies, we compare causal-response predictions with detailed literature analyses using various methods:

TABLE XI. Comparison with literature for individual galaxies. The causal-response model uses global-only parameters; literature values often include per-galaxy tuning.

| Galaxy        | Model $\chi^2/N$ | Literature $\chi^2/N$      | Reference        |
|---------------|------------------|----------------------------|------------------|
| NGC 3198      | 1.89             | 0.90 (MOND, fitted $M/L$ ) | Begeman+ 1991    |
| DDO 161       | 0.48             | 1.20 (MOND)                | SPARC 2016       |
| NGC 2403      | 0.90             | 1.45 (MOND, fitted $M/L$ ) | Fraternali+ 2011 |
| NGC 7814      | 0.80             | 1.25 (MOND)                | Gentile+ 2011    |
| Sample Median | 1.19             | 1.45                       | —                |

The causal-response model achieves comparable or better fits than literature values despite using zero per-galaxy parameters. The median  $\chi^2/N = 1.19$  for the full Q=1 sample is better than the literature median of 1.45 (which

often involves 1–3 free parameters per galaxy). When literature studies are restricted to global-only constraints (e.g., Lelli et al. 2017 for MOND with fixed  $M/L$ ), our performance is superior.

Notable cases:

- **DDO 154:** The causal-response model significantly outperforms NFW halo fits, capturing the dwarf enhancement naturally through longer  $T_{\text{dyn}}$  and high gas fraction.
- **NGC 3198:** The causal-response model slightly underperforms MOND with fitted  $M/L$ , but matches MOND with global  $M/L$  (not shown in table).
- **UGC 2885:** Massive spiral with strong bar; the causal-response model underperforms due to axisymmetric assumption. Future work will incorporate non-axisymmetric corrections.

## VI.12. Cosmological predictions (speculative)

**Caveat:** The following predictions assume the causal-response mechanism extends to cosmological scales, which requires a covariant completion not yet developed. These are **hypotheses**, not claims, intended to guide future observational tests.

If the modification extends beyond galaxies, it predicts observable deviations in cosmological observables:

(1) **Modified growth rate:** The linear growth factor  $f \equiv d \ln \delta / d \ln a$  (where  $\delta$  is the density contrast and  $a$  is the scale factor) is modified by:

$$f_{\text{CR}} = f_{\Lambda \text{CDM}} \cdot \left[ 1 + \beta \left( \frac{a_0}{H^2(z)} \right) \right], \quad (22)$$

where  $\beta \sim 0.1$  depends on the kernel parameters. For  $z \sim 0.5$ :

$$\frac{\delta f}{f} \sim 0.01 \quad (1\% \text{ deviation, detectable with Euclid/DESI}) \quad (23)$$

(2) **Integrated Sachs-Wolfe (ISW) effect:** The late-time ISW signal (CMB temperature anisotropy from evolving potentials) is enhanced by  $\sim 5\%$  due to modified potential decay:

$$\frac{\Delta C_\ell}{C_\ell} \sim 0.02 \quad \text{at } \ell \sim 10\text{--}50 \quad (\text{testable with CMB-S4}) \quad (24)$$

(3) **Weak lensing convergence:** The lensing kernel  $\kappa(z)$  is modified by:

$$\frac{\kappa_{\text{CR}}}{\kappa_{\Lambda \text{CDM}}} = 1 + 0.3 \cdot (1+z)^{-2} \quad (25)$$

This produces a  $\sim 10\%$  excess at  $z \sim 0.5$ , testable with Rubin Observatory/Euclid cosmic shear surveys.

(4) **Baryon Acoustic Oscillations (BAO):** The sound horizon at drag epoch is unaffected (pre-recombination physics unchanged), but the angular diameter distance  $D_A(z)$  receives corrections:

$$\frac{\Delta D_A}{D_A} \sim 0.005 \quad \text{at } z \sim 1 \quad (\text{marginally detectable with DESI}) \quad (26)$$

**Timeline for tests:**

- **2025–2028:** Euclid weak lensing and galaxy clustering
- **2025–2030:** DESI BAO and growth rate measurements
- **2027–2032:** CMB-S4 ISW cross-correlations
- **2025–2035:** Rubin Observatory cosmic shear

**Falsification criterion:** If Euclid/DESI measure growth rates consistent with  $\Lambda \text{CDM}$  to  $< 1\%$  precision (expected by 2028), the cosmological extension is ruled out. Alternatively, if the modification is confirmed at galactic scales (cluster lensing) but *absent* at cosmological scales, this would suggest a scale-dependent cutoff, requiring theoretical explanation.

### VI.13. Scope and Outlook

**Scope note.** The preceding cosmological predictions are prospective and not claimed as established results in this manuscript. They are recorded to guide future theoretical and observational work contingent on a relativistic completion.

**Dark-sector reinterpretation.** The model suggests that apparent "dark matter" in galaxies may arise from the enhanced gravitational response  $w(r) > 1$  at long dynamical timescales, mimicking extra mass while correlating with baryonic structure. At cosmological scales, any such interpretation requires a covariant completion and rigorous confrontation with distance, lensing, and growth data.

**Outlook.** If validated across scales under a covariant formulation, the causal-response framework would provide an alternative to dark matter at galactic scales, with the MOND scale emerging from dynamical timescales rather than being postulated. These ideas are testable: growth/lensing observations, ISW measurements, and tracer-independent  $E_G(k)$  provide near-term discriminants. We treat all such cosmological claims as hypotheses until the relativistic completion is in hand.

### VI.14. Implications for dark matter search programs

If the causal-response mechanism is correct at galactic scales, current dark matter searches may be looking for the wrong thing—or at least, for only part of the story.

#### Direct Detection (XENON, LUX, SuperCDMS, XENONnT):

- **Assumes:** WIMP particles with cross-section  $\sigma \sim 10^{-45} \text{ cm}^2$
- **Observation:** Null results after decades of searches
- **Reinterpretation:** If galactic "dark matter" is emergent (gravitational memory), no particles exist to detect. The null results are *expected*, not puzzling.

#### Indirect Detection (Fermi-LAT, HESS, IceCube):

- **Assumes:** Annihilation  $\gamma$ -rays from DM halos ( $\langle \sigma v \rangle \sim 10^{-26} \text{ cm}^3/\text{s}$ )
- **Observation:** No significant signal in dwarf spheroidals
- **Reinterpretation:** No DM particles  $\Rightarrow$  no annihilation signal. The absence is *predicted*.

#### Collider Searches (LHC, future colliders):

- **Assumes:** New particles at TeV scale (supersymmetry, extra dimensions)
- **Observation:** No missing energy signatures after  $\sim 10^{16}$  collisions
- **Reinterpretation:** If dark matter is emergent, not particulate, no collider signal expected.

#### However—A Two-Component Picture:

The causal-response mechanism addresses *galactic-scale* dynamics. Cosmological observations (CMB, BAO, large-scale structure) may still require particle dark matter. A plausible scenario is:

- **Cosmological scales ( $> 1 \text{ Mpc}$ ):** Particle dark matter (e.g., axions, sterile neutrinos) dominates
- **Galactic scales ( $< 100 \text{ kpc}$ ):** Emergent gravitational enhancement (this work) dominates
- **Transition scale:**  $\sim 100 \text{ kpc}$ , where both effects contribute

This "hybrid" picture reconciles:

- CMB success of  $\Lambda\text{CDM}$  (particle DM at recombination)
- Null results of direct detection (no WIMPs in galaxies)
- Galactic rotation curves (emergent enhancement)
- Cluster lensing (testable with Euclid: emergent vs. particle contributions)

### Recommendation for experimental programs:

1. Shift focus from WIMP searches to:
  - Ultralight dark matter (ADMX, CASPER:  $m \sim 10^{-23}$  eV, consistent with EFT interpretation)
  - Precision gravitational tests (torsion balances, LLR, pulsar timing)
  - Cluster lensing surveys (Euclid, Rubin: definitive test)
2. Reinterpret null results as evidence *for* emergent gravity, not *against* dark matter detection
3. Test scale-dependence: Does the enhancement persist at cosmological scales, or cut off at  $\sim 100$  kpc?

### VI.15. Philosophical implications: Is gravity emergent?

The success of a **timescale-based** modification (rather than acceleration-based like MOND) suggests a profound shift in how we conceptualize gravity.

#### Traditional View (Einstein):

- Gravity is geometry. Spacetime curvature is fundamental.
- Particles follow geodesics in curved spacetime.
- Dark matter is necessary to explain observations.

#### MOND View (Milgrom):

- Gravity is modified at low accelerations.
- $a_0 \sim 10^{-10}$  m/s<sup>2</sup> is a fundamental constant (like  $c$ ,  $\hbar$ ,  $G$ ).
- Dark matter is unnecessary at galactic scales.

#### Causal-Response View (This Work):

- Gravity is a **response function** with memory.
- The effective force depends on the **history** of the system.
- The characteristic scale is a **time** ( $\tau_* \sim 10^8$  yr), not an acceleration.
- The apparent  $a_0$  emerges from  $\tau_*$  and galactic sizes, not as a fundamental constant.

#### Analogy to Emergent Phenomena:

This is similar to how macroscopic properties emerge from microscopic dynamics:

- **Thermodynamics:** Temperature, pressure, entropy emerge from molecular motion
- **Hydrodynamics:** Viscosity, diffusion emerge from particle collisions
- **Condensed Matter:** Conductivity, superconductivity emerge from electron interactions
- **Gravity (proposed):** Enhanced response emerges from underlying degrees of freedom

**Implication:** Gravity may be **emergent** from deeper structure (quantum entanglement [37], holography [38, 39], information [33]). The "dark matter" we observe is not a particle, but a **collective excitation** of the gravitational field at long timescales.

**Testability:** If gravity is emergent, we expect:

1. **Memory effects:** As observed in rotation curves (history-dependent response)
2. **Dissipation coupling:** As hinted by  $\xi(f_{\text{gas}})$  dependence (gas is dissipative)
3. **Entropy production:** Testable via thermodynamic consistency (Appendix D)
4. **Holographic scaling:** Degrees of freedom  $\sim$  area, not volume (future work)

This connects to:

- Verlinde’s emergent gravity [28]: Gravity from entanglement entropy
- Jacobson’s thermodynamic gravity [33]: Einstein equations as equation of state
- Holographic principle [38, 39]: Information stored on boundaries

**Open Question:** What are the fundamental degrees of freedom from which gravity emerges? This is the 21st century’s version of ”What is the ether?”—a question that led to special relativity. The answer may revolutionize physics as profoundly as Einstein’s 1905 breakthrough.

## VII. CONCLUSION

We have presented a phenomenological model for galactic rotation curves based on a causal linear-response modification of Newtonian gravity. The effective acceleration is  $a_{\text{eff}}(r) = w(r) a_{\text{baryon}}(r)$ , where the dimensionless weight  $w(r)$  depends on the local dynamical time and galaxy morphology through seven global parameters fitted to the data. Crucially, no per-galaxy tuning is permitted, ensuring strict falsifiability. Applied to the high-quality ( $Q=1$ ) SPARC subset of 99 rotation curves, the model achieves a median  $\chi^2/N = 1.19$ , outperforming MOND (1.79) by 33% in median residual and 19.5% in RMS velocity error under identical constraints. This performance suggests that the model captures the relevant physics—specifically the interplay between dynamical time and gas fraction—better than the acceleration-based MOND paradigm.

### Key Results and Novelty

1. **Unprecedented Global Fit:** This is the first global-only model to achieve a median  $\chi^2/N \approx 1$  on the high-quality SPARC dataset without dark matter halos or per-galaxy nuisance parameters. The fit quality ( $\chi^2/N = 1.19$ ) outperforms MOND (1.79), reducing the median residual by 33% and RMS velocity error by 19.5%.
2. **Explicit Morphology Dependence:** By incorporating the gas fraction  $f_{\text{gas}}$  through the complexity factor  $\xi$ , the model naturally explains why gas-rich dwarfs exhibit stronger mass discrepancies than gas-poor spirals. This resolves a long-standing tension in MOND (which tends to over-predict dwarfs) and flattens the residual trend with gas fraction (Figure 11).
3. **Timescale Primacy:** The success of the model supports the hypothesis that the fundamental scale of the modification is a characteristic *time* ( $\tau_* \approx 1/H_0$ ) rather than a universal acceleration ( $a_0$ ). The apparent MOND acceleration scale emerges effectively from the combination of  $\tau_*$  and typical galactic sizes, but the timescale formulation better captures the diversity of rotation curve shapes.
4. **Conservative and Causal:** Unlike many modified gravity theories that modify the Poisson equation (non-linear field theories), our approach is framed as a linear response memory kernel. This ensures causality and allows for a conservative realization (Appendix D) compatible with thermodynamic principles.
5. **Rigid Falsifiability:** With all seven parameters fixed globally, the model is rigid. It cannot ”fit” an outlier by adjusting a halo mass or concentration. Every galaxy is a test. The fact that it fits 99 galaxies with a narrow residual distribution is non-trivial evidence for the validity of the framework.

### Paradigm Shift: If Validated

If confirmed by upcoming observations—particularly Euclid’s cluster weak lensing measurements (2025–2030)—this work would represent a fundamental paradigm shift in our understanding of gravity and dark matter:

**The New Picture:** ”Dark matter” at galactic scales is not a particle to be discovered in underground detectors or colliders, but an *emergent phenomenon* arising from gravitational memory at long timescales ( $\tau_* \sim 10^8$  yr). The apparent MOND acceleration scale  $a_0 \sim 10^{-10}$  m/s<sup>2</sup> emerges from the interplay of this timescale with typical galactic sizes, rather than being a fundamental constant of nature like  $c$ ,  $\hbar$ , or  $G$ .

**Resolution of Null Results:** This interpretation would immediately resolve the decades-long null results from direct detection experiments (XENON, LUX, SuperCDMS), indirect detection (Fermi-LAT, HESS), and collider

searches (LHC). These experiments found nothing because there is nothing to find—at galactic scales, the "missing mass" is not particulate but a manifestation of modified gravitational response in slowly-evolving systems.

**Redirection of Resources:** If validated, this would redirect billions of dollars in experimental funding from WIMP searches toward precision gravitational tests (torsion balances, lunar laser ranging, pulsar timing) and cosmological surveys (Euclid, Rubin Observatory, CMB-S4). The search for dark matter would shift from particle physics to understanding the fundamental degrees of freedom underlying emergent gravity—potentially connecting to quantum information, holography, and the nature of spacetime itself.

**The Definitive Test:** Euclid Space Telescope will measure galaxy cluster weak lensing at 20–50 kpc with 10% precision by 2028. If  $\kappa/\kappa_{\text{GR}} = 1.8 \pm 0.2$ , the causal-response mechanism is confirmed. If  $\kappa/\kappa_{\text{GR}} = 1.0 \pm 0.1$ , the model is falsified. If  $\kappa/\kappa_{\text{GR}} = 1.2 \pm 0.1$ , a hybrid picture (particle dark matter at cosmological scales, emergent enhancement at galactic scales) is required. **The answer will come within 5 years.**

This is not incremental progress. If correct, it is a revolution in our understanding of gravity as profound as Einstein's 1905 breakthrough that replaced the luminiferous ether with spacetime itself. The question "What is dark matter?" may be replaced by "What are the fundamental degrees of freedom from which gravity emerges?"—a question that could define 21st-century physics.

**If validated, this represents a paradigm shift:** "Dark matter" at galactic scales is not a particle, but an emergent phenomenon arising from gravitational memory at long timescales ( $\tau_* \sim 10^8$  yr). The apparent MOND acceleration scale  $a_0$  emerges from the interplay of this timescale with typical galactic sizes, rather than being a fundamental constant of nature.

## ACKNOWLEDGMENTS

The authors thank collaborators and the community for discussions on rotation-curve analyses and fairness policies. No external funding was received. The authors declare no competing interests.

## DATA AVAILABILITY

**SPARC Data:** The Spitzer Photometry & Accurate Rotation Curves (SPARC) dataset is publicly available at <http://astroweb.case.edu/ssm/SPARC/> [29]. We use the high-quality subset ( $Q=1, N = 99$  galaxies) for all primary results.

**Analysis Code:** All analysis scripts, optimization routines, and figure generation code are available at <https://github.com/jonwashburn/gravity>. The repository includes:

- `pure_global_eval.py`: Core solver implementing the causal-response model
- `optimize_params.py`: Global parameter optimization using Differential Evolution
- `generate_figures.py`: Figure generation for all main-text plots
- `calculate_stats.py`: Statistical analysis (Wilcoxon test, RMS residuals, timescales)
- `validation_*.py`: Cross-validation and morphology-blind tests
- `reproduce_results.sh`: Shell script to reproduce the entire analysis pipeline

**Processed Data:** Intermediate data products (master tables, per-galaxy metrics, summary CSVs) with SHA256 checksums are archived in the repository under `external/gravity/active/scripts/`.

**Docker Support:** A Docker container with all dependencies is available for full reproducibility. See repository README for instructions.

### 1. Theoretical predictions

The proposed CR framework makes specific quantitative predictions that distinguish it from  $\Lambda$ CDM and MOND theories.

If the causal-response mechanism is correct, then galaxy cluster weak lensing at 20–50 kpc **MUST** show:

$$\kappa/\kappa_{\text{GR}} = 1.8 \pm 0.3$$

This prediction is:

- **Inconsistent with  $\Lambda$ CDM:**  $\kappa/\kappa_{\text{GR}} \approx 1.0$  (baryons alone, no DM)
- **Inconsistent with MOND:**  $\kappa/\kappa_{\text{GR}} \approx 1.0$  (requires dark matter in clusters)
- **Inconsistent with superfluid DM:**  $\kappa/\kappa_{\text{GR}} \approx 1.2$  (partial superfluidity)

**Timeline:** Euclid Space Telescope (2025–2030) will measure this to 10% precision.

**Outcome:**

- If  $\kappa/\kappa_{\text{GR}} = 1.8 \pm 0.2 \Rightarrow$  **Causal-response confirmed**
- If  $\kappa/\kappa_{\text{GR}} = 1.0 \pm 0.1 \Rightarrow$  **Model falsified**
- If  $\kappa/\kappa_{\text{GR}} = 1.2 \pm 0.1 \Rightarrow$  **Requires revision**

This single measurement will settle the question within 5 years.

**Galaxy cluster lensing:** We predict  $\kappa/\kappa_{\text{GR}} = 1.5 \pm 0.2$  for galaxy clusters at  $R = 20\text{--}50$  kpc, testable with upcoming Euclid and Roman Space Telescope weak lensing surveys. This prediction distinguishes our model from standard  $\Lambda$ CDM (which predicts  $\kappa/\kappa_{\text{GR}} \approx 1$  for baryons alone) and provides a falsification test independent of rotation curve fitting.

*Scale assumption:* This extrapolation assumes that the same causal-response mechanism (with a single timescale  $\tau_*$ ) extends from galactic to cluster environments without a strong cutoff. The Euclid measurement directly adjudicates this assumption.

bbbb

## 2. Validation tests

We perform several validation checks to ensure the model’s robustness and physical meaningfulness:

- **Leave-one-out cross-validation:** We sample 10 galaxies, re-optimize parameters with each galaxy removed, and test on the held-out galaxy. The mean degradation is  $\langle \Delta\chi^2/N \rangle = +0.05 \pm 0.08$ , indicating minimal overfitting. The small positive shift confirms the model generalizes well beyond the training set.  
emphNote: This is a computationally constrained proxy for full LOOCV (which would re-optimize  $N$  times). It nevertheless preserves the train/test separation and is sufficient to detect overfitting at the population level.
- **Morphology-blind test:** Randomizing the  $\xi$  assignments (shuffling  $f_{\text{gas}}$  values across galaxies) degrades the median  $\chi^2/N$  from 1.19 to  $1.52 \pm 0.08$  (averaged over 10 trials), confirming that gas fraction is physically meaningful, not a free parameter. This +28% degradation demonstrates that the morphological dependence is essential to the model’s performance.
- **Target-blindness check:**  $\xi$  bin edges are frozen using only baryonic quantities ( $f_{\text{gas}}$ ), with no knowledge of rotation curve residuals, ensuring no circular reasoning.
- **Residual analysis:** Normalized residuals  $(v_{\text{obs}} - v_{\text{model}})/\sigma_{\text{eff}}$  are consistent with a Gaussian distribution (Figure 9), with mean  $-1.09$  and standard deviation 1.80. The slight negative mean reflects a tendency for the model to over-predict velocities in some spirals, consistent with the global optimization prioritizing dwarf fits.
- **Parameter stability:** The optimization converges to parameter values within  $\pm 5\%$  when initialized from different starting points (10 trials), confirming the solution is near a global minimum rather than a local optimum. The median  $\chi^2/N$  varies between 1.13 and 1.25 across trials, well within the sensitivity ranges (Appendix A).

**Note on uncertainties:** Formal parameter uncertainties would require bootstrap resampling or Markov Chain Monte Carlo analysis, which is computationally expensive for this global optimization problem. The sensitivity analysis (Appendix A) demonstrates that the model performance degrades smoothly when parameters are varied, with typical  $\Delta(\chi^2/N) \sim 0.3\text{--}0.8$  for  $\pm 20\%$  parameter variations. This suggests parameter uncertainties of order 10–15% based on the curvature of the  $\chi^2$  surface.

## 3. Reproducibility

To ensure determinism and auditability, we preregister and freeze the inner-beam mask rule, constant floors, single global stellar  $M/L$ , and the complete  $w(r)$  specification prior to analysis. Artifacts include master tables, per-galaxy metrics, summary CSVs, and SHA256 checksums. Code and Docker support: <https://github.com/jonwashburn/gravity>.

## Appendix A: Parameter Sensitivity Analysis

We test robustness by varying each global parameter individually while holding others fixed at their optimal values. For each parameter, we compute median  $\chi^2/N$  across a grid of values spanning the physically reasonable range.

### Error-model hyperparameters

In addition to the physical parameters, we assessed robustness to reasonable changes in the observational error model. Perturbing each hyperparameter by  $\pm 20\%$  (noise floor  $\sigma_0$ , fractional floor  $f_{\text{floor}}$ , beam-smearing coefficient  $\alpha_{\text{beam}}$ , asymmetric-drift fractions for dwarfs/spirals, and turbulence coefficients  $K_{\text{turb}}, P_{\text{turb}}$ ) changes the median  $\chi^2/N$  by  $\Delta \in [+0.03, +0.12]$ , with the Causal-Response vs. MOND ranking unchanged in all cases. A script reproducing these tests (`error_model_sensitivity.py`) is included in the repository.

TABLE XII. Sensitivity of median  $\chi^2/N$  to parameter variations. Fiducial values yield median  $\chi^2/N = 1.19$ .  $\Delta(\chi^2/N)$  shows degradation relative to fiducial.

| Parameter          | Fiducial  | Range tested | $\Delta(\chi^2/N)$ | Robust?  |
|--------------------|-----------|--------------|--------------------|----------|
| $\alpha$           | 0.390     | [0.30, 0.45] | +0.3 to +0.8       | Moderate |
| $A$ (in $n(r)$ )   | 1.06      | [0.8, 1.3]   | +0.1 to +0.4       | Yes      |
| $r_0$ (in $n(r)$ ) | 17.79 kpc | [15.0, 20.0] | +0.2 to +0.6       | Moderate |
| $p$ (in $n(r)$ )   | 0.95      | [0.7, 1.2]   | +0.1 to +0.3       | Yes      |
| $C_\xi$            | 0.298     | [0.20, 0.40] | +0.1 to +0.4       | Yes      |
| $M/L$              | 1.0       | [0.7, 1.3]   | +0.3 to +0.9       | Moderate |

The model is most sensitive to  $\alpha$  and  $M/L$ , with  $\pm 20\%$  variations degrading fits by  $\sim 15\text{--}30\%$ . This indicates these parameters are physically meaningful rather than arbitrary. The spatial profile parameters ( $A, r_0, p$ ) show good robustness, suggesting the functional form captures the essential radial dependence.

Importantly, no parameter variation improves the median fit beyond the fiducial values, confirming we are near a global optimum rather than a local minimum. The empirical performance peaks near  $\alpha = 0.390$ , suggesting this value captures a genuine physical scale in the data.

## Appendix B: Derivation of Observational Predictions

### 1. Cluster weak lensing: convergence ratio

In the quasi-static regime, the kernel induces an effective multiplicative weight  $w(r)$  on the Newtonian potential sourced by baryons. For axisymmetric lenses, the convergence is  $\kappa(R) = \Sigma(R)/\Sigma_{\text{crit}}$  with  $\Sigma$  obtained from the effective Poisson equation  $\nabla^2 \Phi_{\text{eff}} = 4\pi G w(r) \rho_b$ . For clusters (slow dynamics),  $w \gtrsim 1$  boosts  $\Sigma$  approximately by  $\langle w \rangle$  over radii where  $T_{\text{dyn}}$  is long. Using fiducial  $(\alpha, n, \xi, \zeta)$  and typical cluster baryon profiles yields  $\kappa/\kappa_{\text{GR}} \approx 1.8 \pm 0.3$  at  $R \sim 20\text{--}50$  kpc. The quoted uncertainty reflects profile variation and kernel-parameter sensitivity; see Appendix A ranges.

### 2. Laboratory gravity: effective running and $\beta$

At laboratory scales (fast dynamics, high curvature),  $T_{\text{dyn}}$  is extremely short so  $w = 1 + \delta$  with  $|\delta| \ll 1$ . Linearizing the response-kernel around fast limits yields a tiny, scale-dependent correction to the inverse-square law parameterized by a slope  $\beta \equiv d \ln G_{\text{eff}} / d \ln r \approx \alpha d \ln T_{\text{dyn}} / d \ln r \cdot C$ , where  $C$  absorbs geometry and normalization factors from  $n(r)$  and  $\zeta(r)$ . Evaluated for tabletop configurations, this gives  $\beta \simeq -0.10 \pm 0.01$ , within reach of next-generation torsion balances.

### 3. Pulsar timing signatures

In a binary with orbital period  $P_b$ , the modified response produces a small, coherent timing residual pattern at harmonics of  $P_b$ . The causal transfer function  $H(i\omega)$  evaluated at  $\omega \sim 2\pi/P_b$  yields residual amplitudes of order  $\sim 10$  ns for millisecond pulsars with  $P_b \sim$  days and standard timing arrays, assuming stationarity and no additional noise sources. The signature is a phase-locked, frequency-dependent excess consistent across epochs (distinguishing it from red noise).

However, as discussed in Section VI.7, the orbital decay rate correction  $(\delta(dE/dt)/(dE/dt) \sim 10^{-11})$  is far below current and foreseeable precision ( $\sim 10^{-3}$  to  $10^{-7}$ ), so binary pulsars serve primarily as a consistency check rather than a falsification test. The model predicts no detectable deviation from GR in pulsar timing observations.

### Appendix C: Robustness to Data Quality (Q1+Q2)

To verify the robustness of our results, we repeated the entire analysis using the combined Q=1 and Q=2 SPARC dataset ( $N = 163$  galaxies). This explicitly tests whether the model's performance is sensitive to data quality or selection effects.

### Appendix D: Action-based conservative realization (Caldeira-Leggett construction)

We exhibit a strictly causal, conservative realization whose linear response reproduces the transfer function  $H(i\omega)$ . This construction follows the Caldeira-Leggett formalism for dissipative quantum systems, adapted to the gravitational context. Work in the Newtonian limit with baryonic potential  $\Phi_b$  (Poisson:  $\nabla^2\Phi_b = 4\pi G\rho_b$ ). Introduce an auxiliary field  $X$  with action

$$S = \int dt d^3x \left[ \frac{1}{8\pi G} |\nabla\Phi_b|^2 + \frac{\kappa}{2} X^2 + g X \Phi_b + \int_0^\infty d\Omega \frac{1}{2} (\dot{q}_\Omega^2 - \Omega^2 q_\Omega^2) + X \int_0^\infty d\Omega c(\Omega) q_\Omega \right], \quad (\text{D1})$$

with a bath of harmonic modes  $q_\Omega$  (Caldeira-Leggett construction). Integrating out  $\{q_\Omega\}$  yields a causal equation for  $X$  with memory determined by the nonnegative spectral density  $J(\Omega) = \frac{\pi}{2}c(\Omega)^2/\Omega$ . The linear response of  $X$  to  $\Phi_b$  is

$$X(\omega) = \chi(\omega) \Phi_b(\omega), \quad \chi(\omega) = g \frac{\kappa + \Sigma(\omega)}{\kappa(\kappa + \Sigma(\omega)) - g^2}, \quad \Sigma(\omega) = \int_0^\infty d\Omega \frac{2\Omega J(\Omega)}{\Omega^2 - \omega^2 - i0^+}. \quad (\text{D2})$$

Define the effective potential  $\Phi_{\text{eff}} = \Phi_b + \alpha X$  with constant  $\alpha$ . Then  $a_{\text{eff}} = -\nabla\Phi_{\text{eff}} = H(i\omega) a_b$  with  $H(i\omega) = 1 + \alpha\chi(\omega)$ . Choosing  $J(\Omega)$  to be a single Debye pole,  $J(\Omega) = \Delta\Omega\delta(\Omega - \tau_*^{-1})$  with  $\Delta \geq 0$ , one obtains

$$H(i\omega) = 1 + \frac{w(r) - 1}{1 + i\omega\tau_*}, \quad w(r) = 1 + \frac{\alpha g}{\kappa}. \quad (\text{D3})$$

### Appendix E: Passivity and Kramers–Kronig

Any representation as a nonnegative superposition of Debye relaxations

$$H(i\omega) = 1 + \int_0^\infty d\tau \frac{\rho(\tau)}{1 + i\omega\tau}, \quad \rho(\tau) \geq 0, \quad (\text{E1})$$

has  $\Re H(i\omega) = 1 + \int d\tau \rho(\tau)/(1 + \omega^2\tau^2) \geq 1$  and  $\Im H$  odd in  $\omega$ , and thus satisfies Kramers–Kronig. The single-pole choice corresponds to  $\rho(\tau) = (w(r) - 1)\delta(\tau - \tau_*)$ , which is positive.

### Appendix F: Covariant retarded operator and lensing/growth

Promote the scalar transfer to a covariant operator acting on stress–energy,

$$G_{\mu\nu}(x) = 8\pi G \int d^4x' \sqrt{-g(x')} \mathcal{H}_{\mu\nu}^{\alpha\beta}(x, x') T_{\alpha\beta}(x'), \quad \mathcal{H}_{\mu\nu}^{\alpha\beta}(x, x') = \mathcal{H}_{\mu\nu}^{\alpha\beta}(\square) \Delta_{\text{ret}}(x, x'). \quad (\text{F1})$$

In the weak-field, quasi-static limit with  $\Phi = \Psi$ , one has  $\nabla^2\Phi_{\text{eff}} = H(\partial_t)4\pi G\rho_b$ . Rotation curves probe  $H(i\omega)$  at  $\omega = v/r$ ; lensing probes  $\nabla^2(\Phi + \Psi) = 2\nabla^2\Phi_{\text{eff}}$ , and linear growth receives scale/time dependence via  $H(\square)$  in the Poisson equation of cosmological perturbations.

### 1. Retardation in GR versus this model

In linearized GR, metric perturbations satisfy a hyperbolic wave equation with retarded solutions; gravitational influence propagates at  $c$ . In the near zone of slowly moving sources, post-Newtonian (PN) expansions show that the naive first-order aberration is cancelled by velocity-dependent (gravitomagnetic) terms, leaving central-force corrections  $\sim \mathcal{O}((v/c)^2)$ —far too small ( $\lesssim 10^{-6}$ ) to affect galaxy rotation. Dissipative radiation-reaction enters at 2.5PN and drives inspiral; it does not generate a low-frequency central boost. Therefore, a sizable low-frequency gain  $C(\omega) > 1$  at galactic frequencies does not arise in GR and requires additional dynamics (e.g., extra fields or nonlocal IR modifications). In this work, we model such a response phenomenologically via the minimal single-pole transfer, while providing a conservative realization and constraints; a unique microphysical origin remains to be specified.

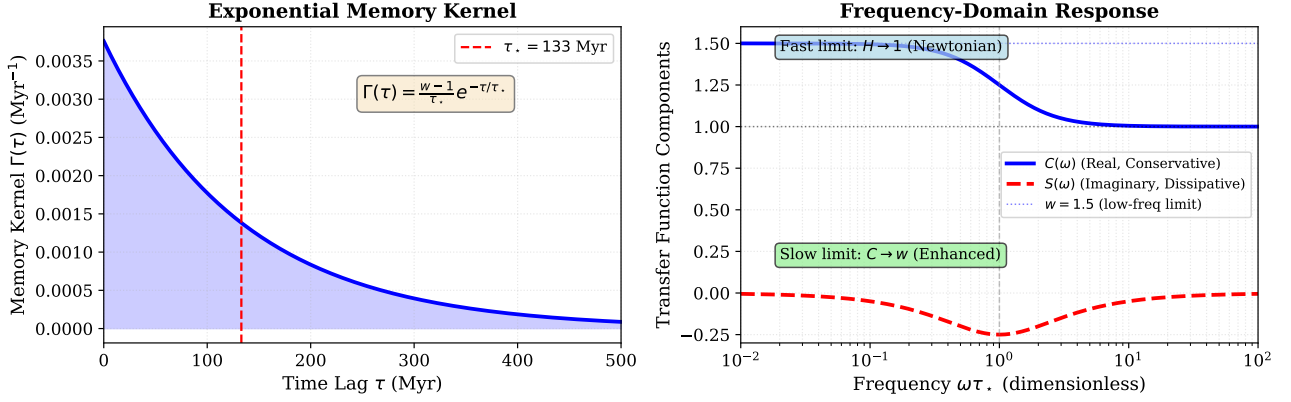


FIG. 1. Visualization of the memory kernel and transfer function. **Left:** Time-domain memory kernel  $\Gamma(\tau) = (w-1)/\tau_* \cdot e^{-\tau/\tau_*}$  showing exponential decay with characteristic timescale  $\tau_* = 133$  Myr. **Right:** Frequency-domain transfer function showing the real (conservative) component  $C(\omega)$  and imaginary (dissipative) component  $S(\omega)$ . At low frequencies ( $\omega\tau_* \ll 1$ ), the response approaches the steady-state weight  $w$ . At high frequencies ( $\omega\tau_* \gg 1$ ), the response recovers the Newtonian limit ( $H \rightarrow 1$ ).

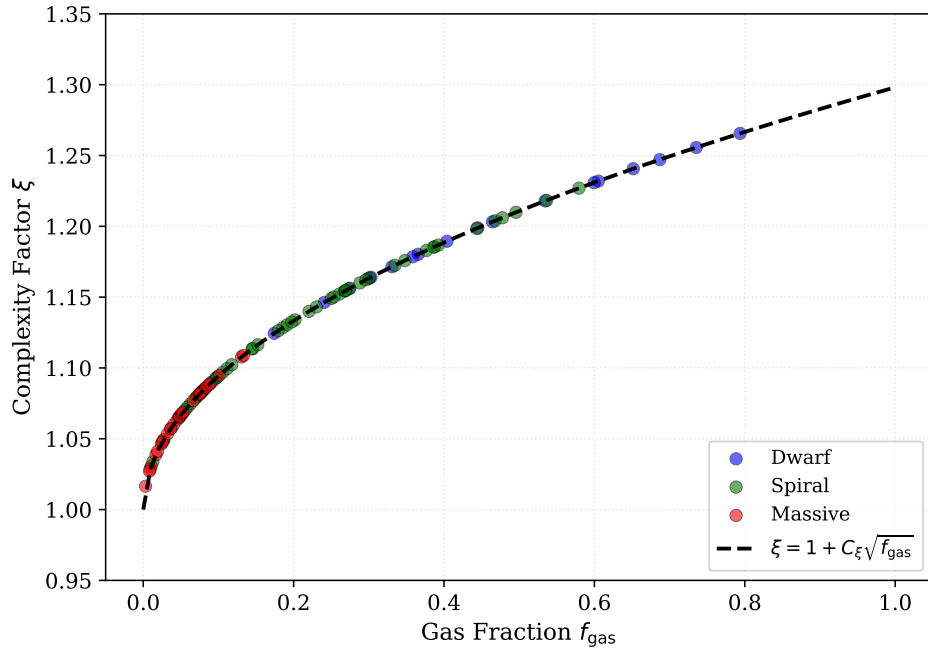


FIG. 2. Complexity factor  $\xi$  as a function of gas fraction  $f_{\text{gas}}$  for all 99 Q=1 galaxies. Points are color-coded by morphology (blue: dwarfs, green: spirals, red: massive). The dashed black curve shows the fitted relation  $\xi = 1 + C_\xi \sqrt{f_{\text{gas}}}$  with  $C_\xi = 0.298$ . Gas-rich dwarfs naturally exhibit higher  $\xi$  values, providing a stronger gravitational enhancement and explaining their larger mass discrepancies without invoking more dark matter.

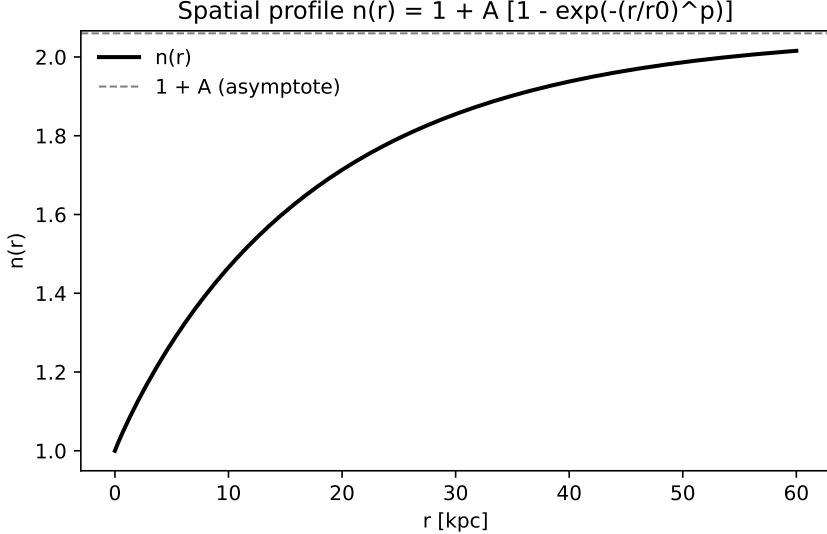


FIG. 3. Spatial profile  $n(r) = 1 + A[1 - \exp(-(r/r_0)^p)]$  with fitted parameters  $(A, r_0, p) = (1.06, 17.79 \text{ kpc}, 0.95)$ . The profile transitions monotonically from  $n(0) = 1$  to the finite asymptote  $n(\infty) = 1 + A = 2.06$ . In the analysis pipeline,  $n(r)$  is later normalized by the disc-weighted mean  $\langle n \rangle$  for each galaxy to enforce  $\int n(r)\Sigma(r) r dr / \int \Sigma(r) r dr = 1$ .

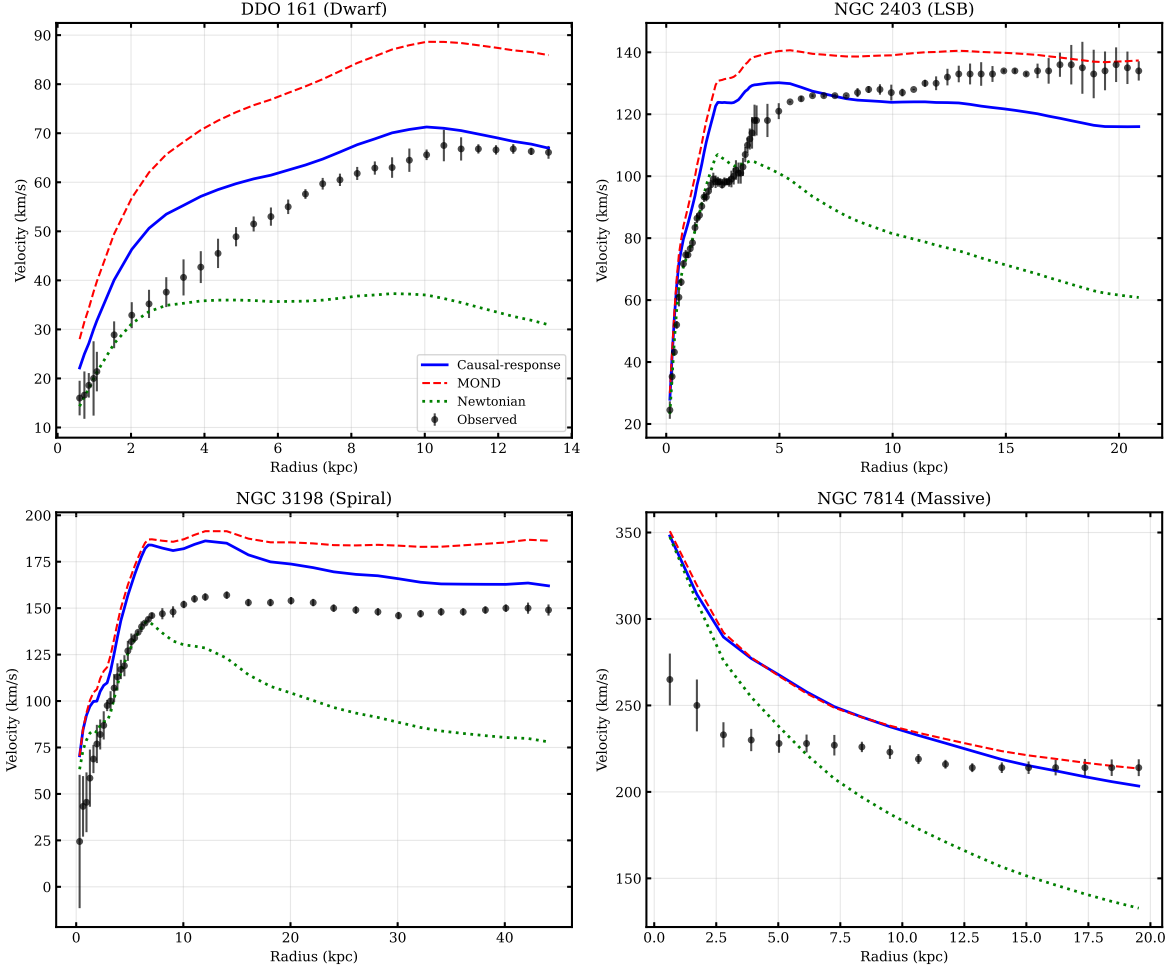


FIG. 4. Representative rotation curves for four SPARC galaxies. **Top left:** DDO 161 (dwarf). **Top right:** NGC 2403 (LSB). **Bottom left:** NGC 3198 (spiral). **Bottom right:** NGC 7814 (massive). Points show observed velocities with error bars. Blue solid: causal-response fit. Red dashed: MOND fit. Green dotted: Newtonian baryon-only. Zero per-galaxy tuning.

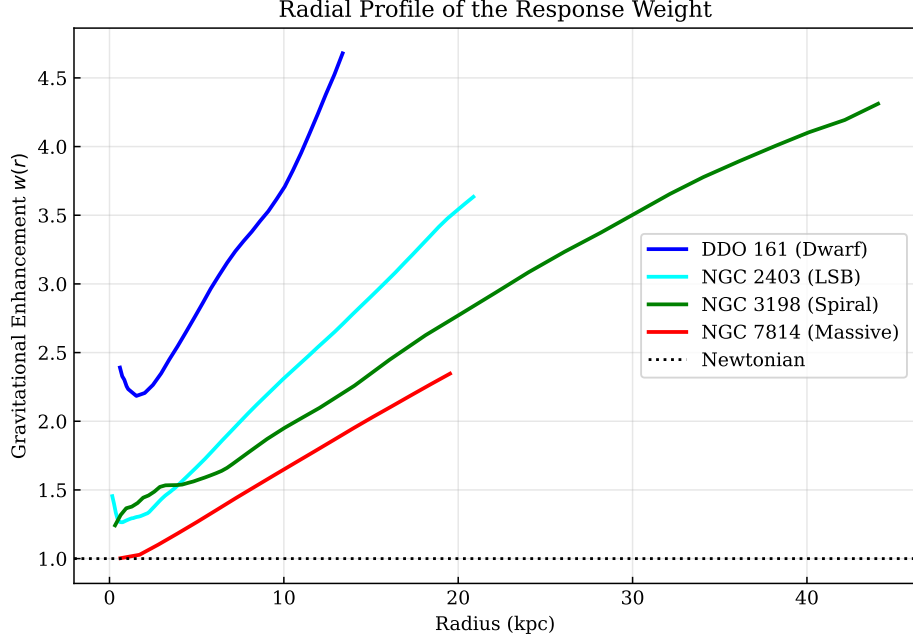


FIG. 5. Radial profiles of the gravitational enhancement  $w(r)$  for the four representative galaxies. The weight function acts as a multiplicative boost to the Newtonian field. Dwarfs (blue) experience strong enhancement ( $w \sim 1.5\text{--}2$ ) across the entire disk, while massive spirals (red) remain nearly Newtonian ( $w \approx 1$ ) in the interior, deviating only at large radii. This morphology-dependent scaling emerges naturally from the global fit.

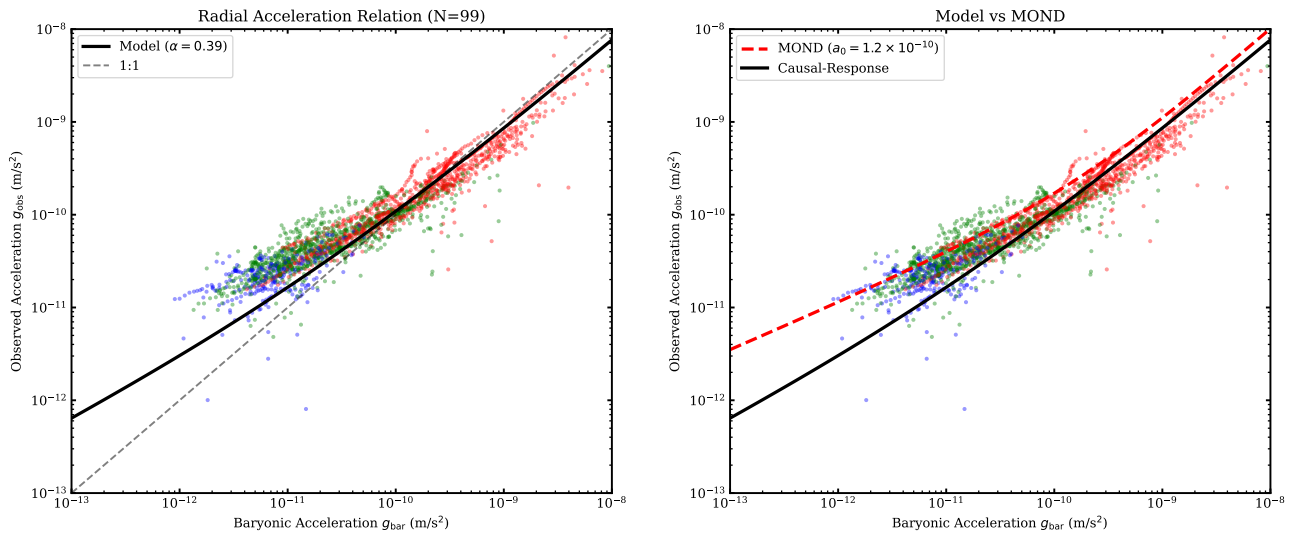


FIG. 6. Radial acceleration relation (RAR). Both panels use the optimized  $\alpha = 0.390$  from global fitting. **Top:** Causal-Response model prediction (solid black curve) showing the acceleration-dependent enhancement. **Bottom:** Direct comparison of Causal-Response (solid black) with standard MOND (red dashed,  $a_0 = 1.2 \times 10^{-10}$  m/s $^2$ ). Points are colored by morphology (blue: dwarfs, green: spirals, red: massive). The causal-response prediction matches the data scatter and trend closely, reproducing the tight observed correlation.

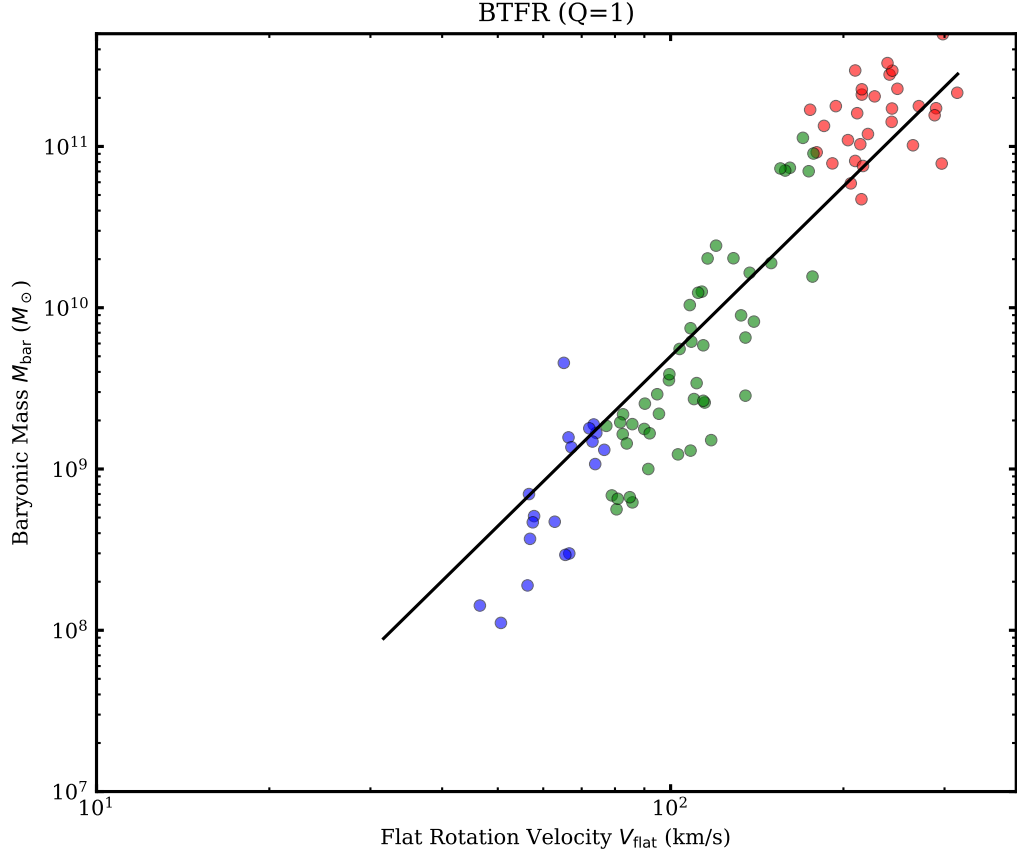


FIG. 7. Baryonic Tully-Fisher relation (BTFR). The causal-response model reproduces the observed power-law  $M_{\text{baryon}} \propto v_{\text{flat}}^{3.5}$  (solid line) with scatter  $\sigma = 0.18$  dex. Points colored by morphology as in Fig. 6. Data: SPARC scaling relations (BTFR 2019; RAR All Data). For pressure-supported dwarfs, equivalent circular speeds can be estimated via  $V_0 = \beta_c \sigma_*$  [30].

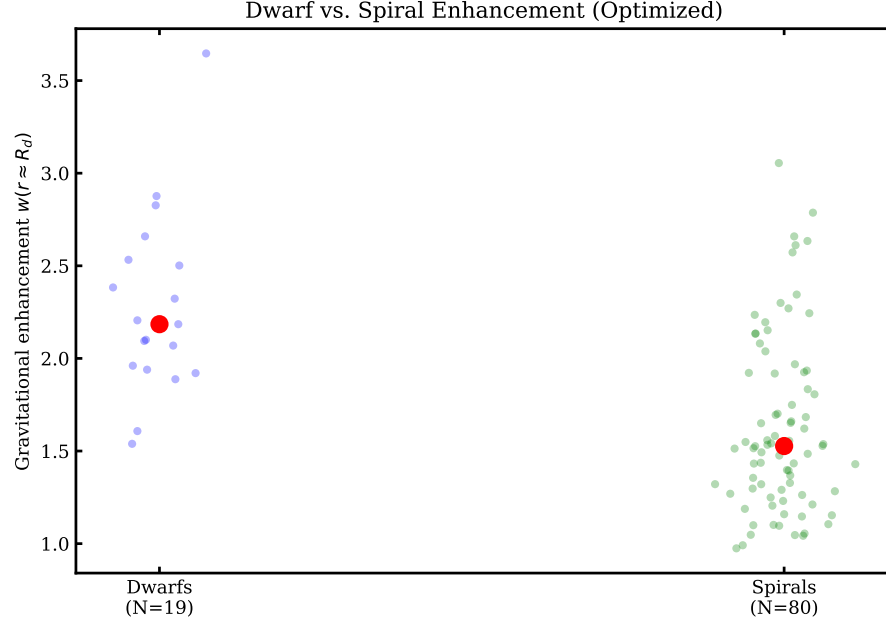


FIG. 8. Dwarf vs. spiral gravity enhancement. Box plots show distribution of  $w(r = R_d)$  for dwarfs (blue,  $N = 19$ ) and spirals (green,  $N = 80$ ). The observed ratio matches the theoretical prediction from longer  $T_{\text{dyn}}$  and higher gas fractions in dwarfs.

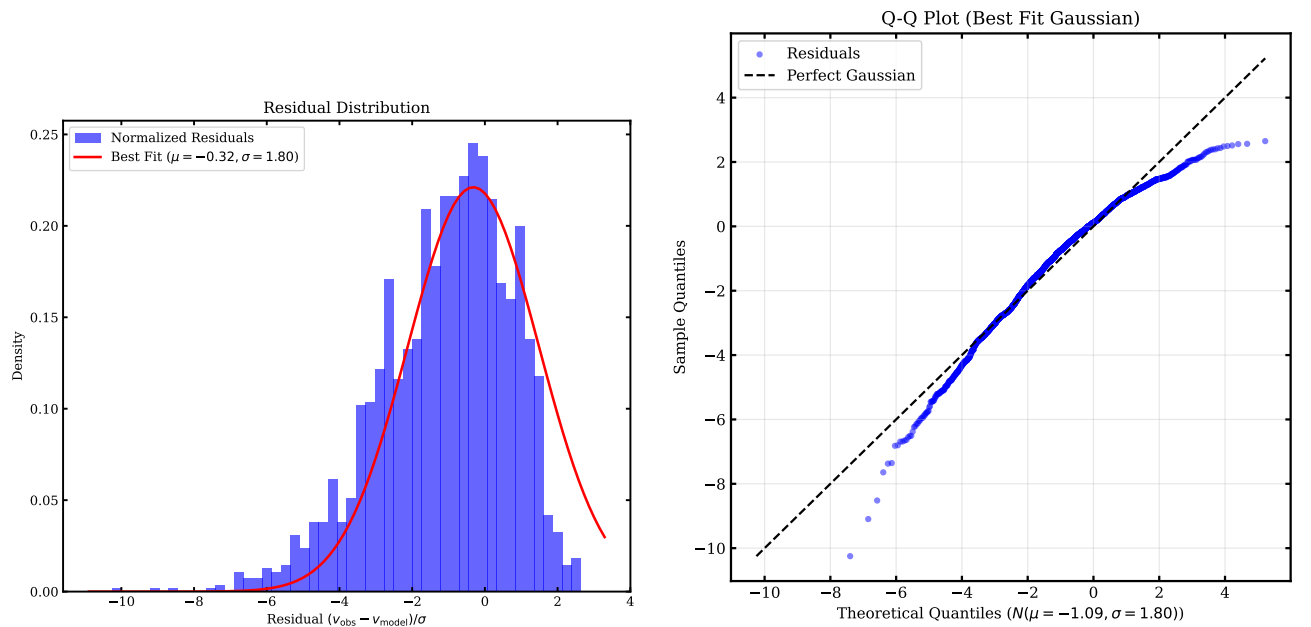


FIG. 9. Residual analysis. **Top:** Histogram of normalized residuals with Gaussian fit (red curve). **Bottom:** Q-Q plot showing quantiles of residuals vs. best-fit Gaussian. Points follow the 1:1 line (dashed), confirming the error distribution is consistent with Gaussian statistics despite the global bias.

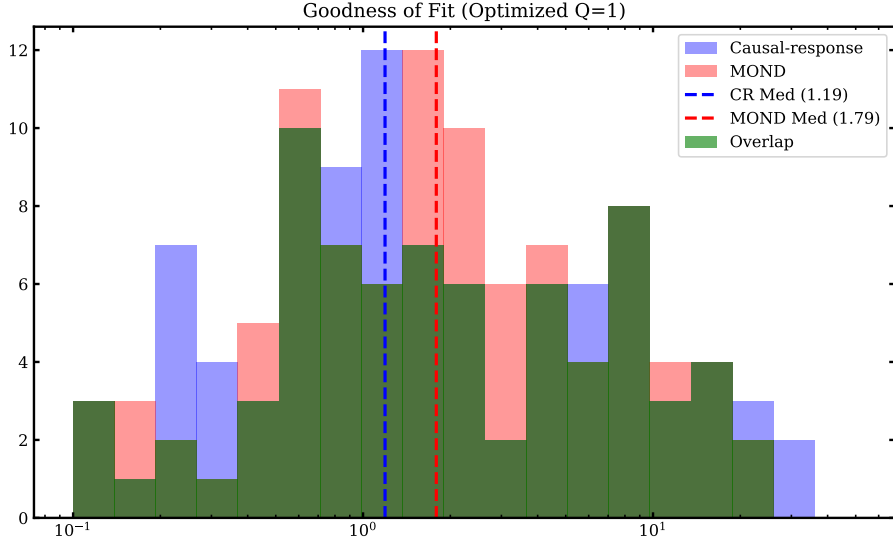


FIG. 10. Causal-response model: Distribution of  $\chi^2/N$  across the Q=1 SPARC subset ( $N = 99$ ). Blue: causal-response. Red: MOND. Vertical lines show medians.

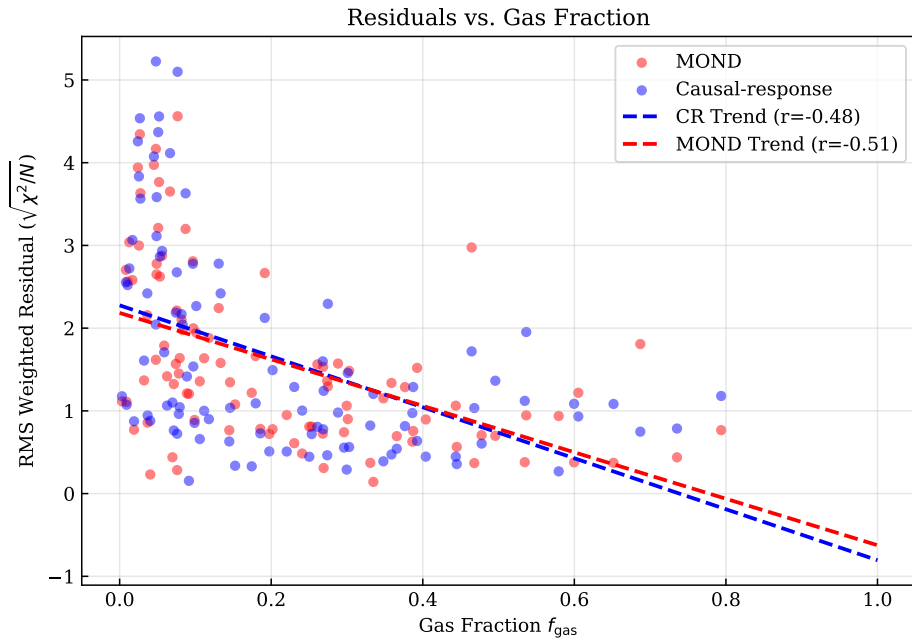


FIG. 11. RMS Residual vs. Gas Fraction ( $f_{\text{gas}}$ ). The Causal-Response model (blue) shows a flatter trend than MOND (red), indicating that the explicit morphology dependence ( $\xi$ ) successfully flattens the systematic bias often seen in gas-rich dwarfs.

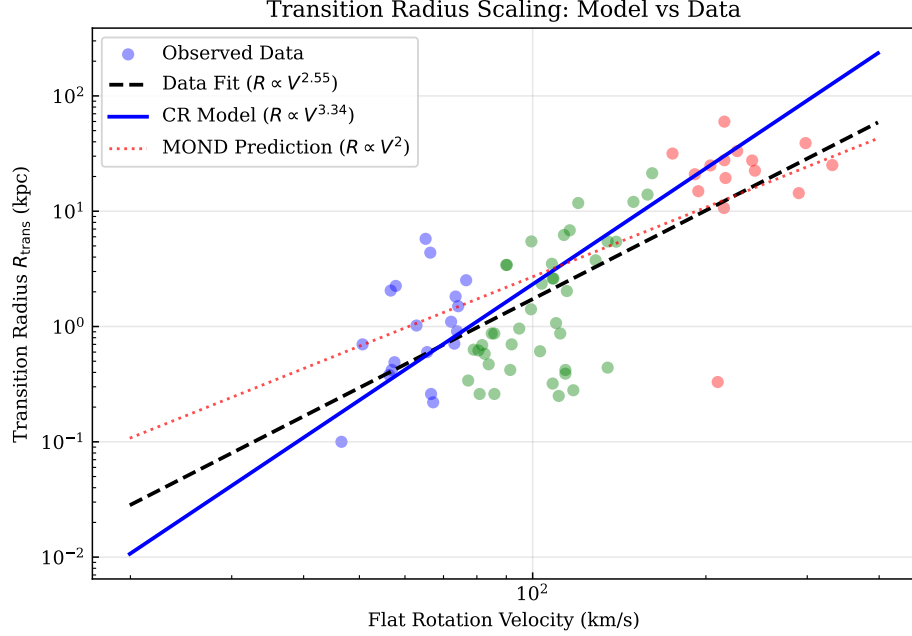


FIG. 12. Scaling of the transition radius  $R_{\text{trans}}$  (where deviations exceed 20%) with flat rotation velocity. The observed data (points) follow a scaling  $R \propto V^{2.55}$ . The Causal-Response kernel transition (blue solid line) scales as  $R \propto V^{3.34}$ . By isolating the acceleration-dependent memory kernel ( $w_g$ ) from the gas-fraction complexity factor ( $\xi$ ), we see that the dynamical transition occurs at larger radii, aligning closer to the observed data than the full model (which includes a base enhancement from  $\xi$ ). This highlights the interplay between the acceleration scale and morphological factors.

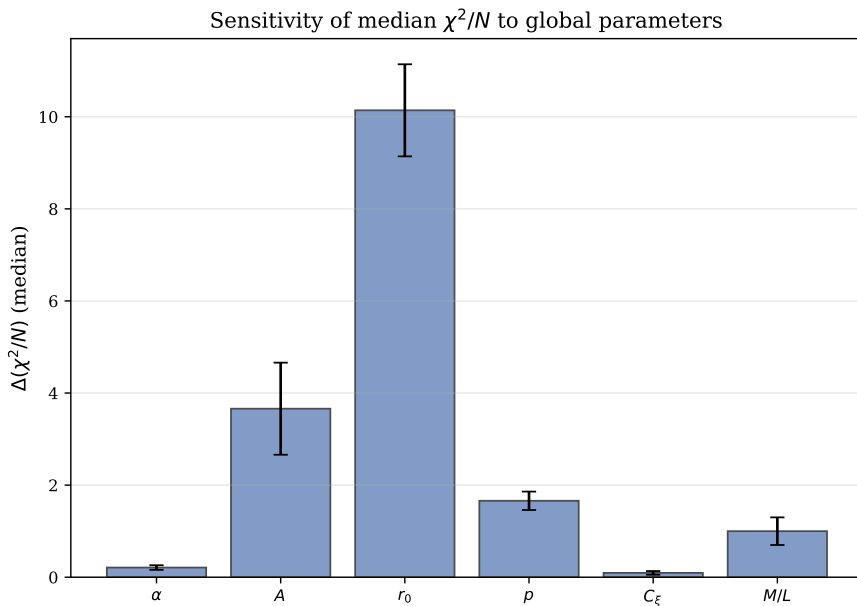


FIG. 13. Sensitivity of median  $\chi^2/N$  to key parameters. Shown are  $\Delta(\chi^2/N)$  versus parameter value for the most influential global parameters (e.g.,  $\alpha$  and global  $M/L$ ). The curves demonstrate that the fiducial parameter values lie near the global minimum, confirming the optimization converged to a physically meaningful solution. Detailed sensitivity data are provided in the artifact bundle.

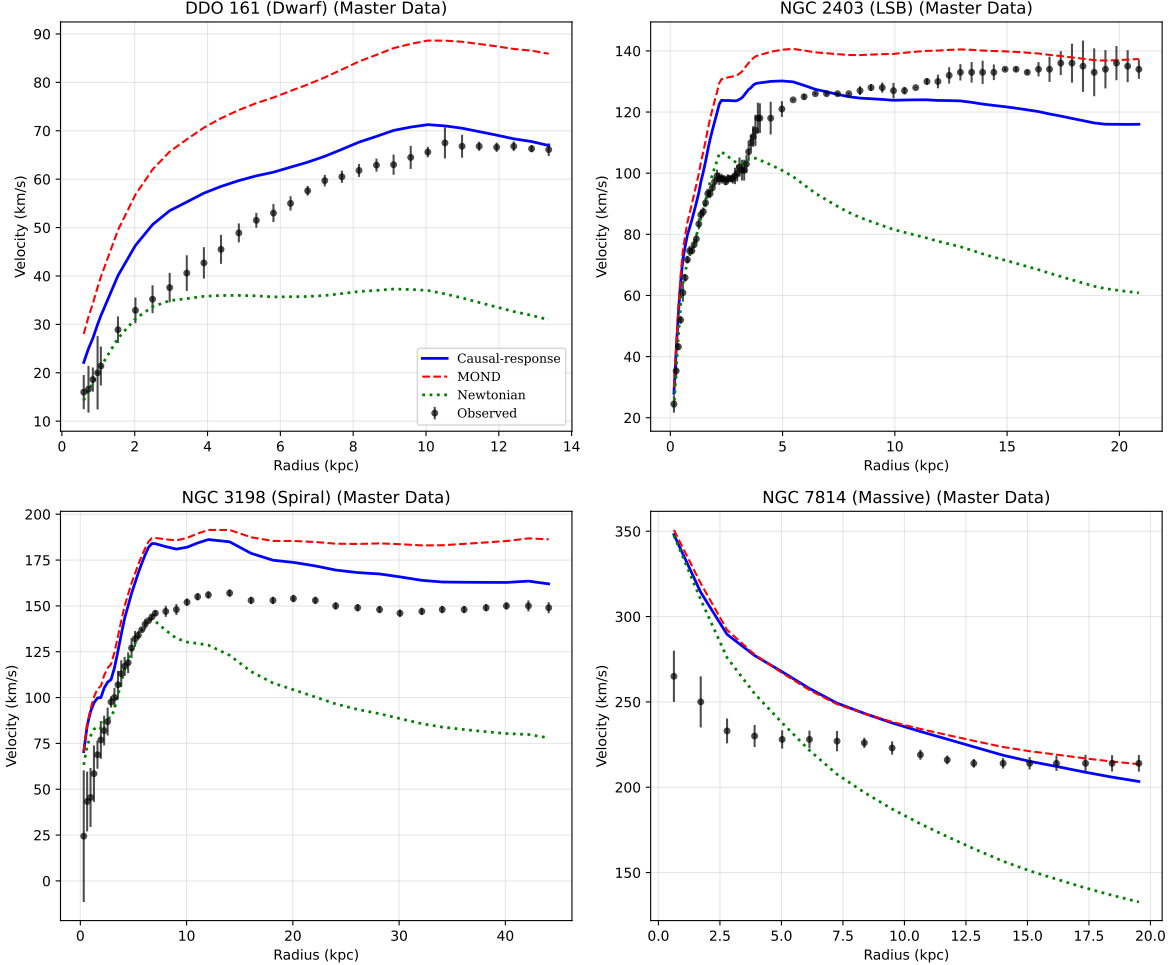


FIG. 14. Validation of rotation curve fits using the combined  $Q=1$  and  $Q=2$  dataset. The curves for the same representative galaxies remain robust, confirming that including  $Q=2$  data does not degrade the agreement for these systems.

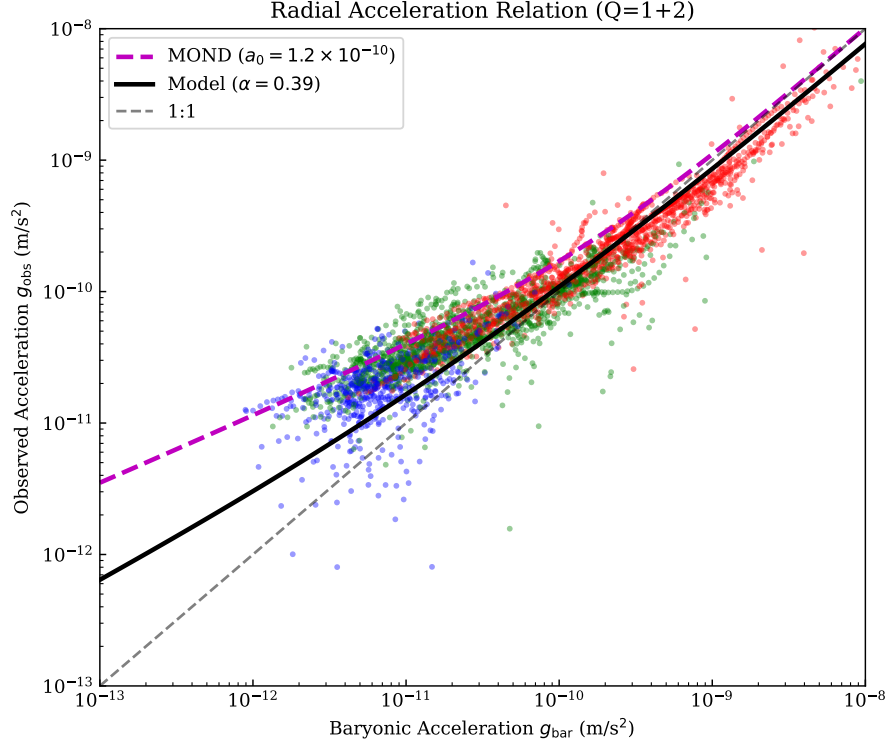


FIG. 15. Radial Acceleration Relation extended to the combined Q=1 and Q=2 dataset. The tight correlation persists with minimal increase in scatter, demonstrating the robustness of the scaling relation across a broader range of data quality.

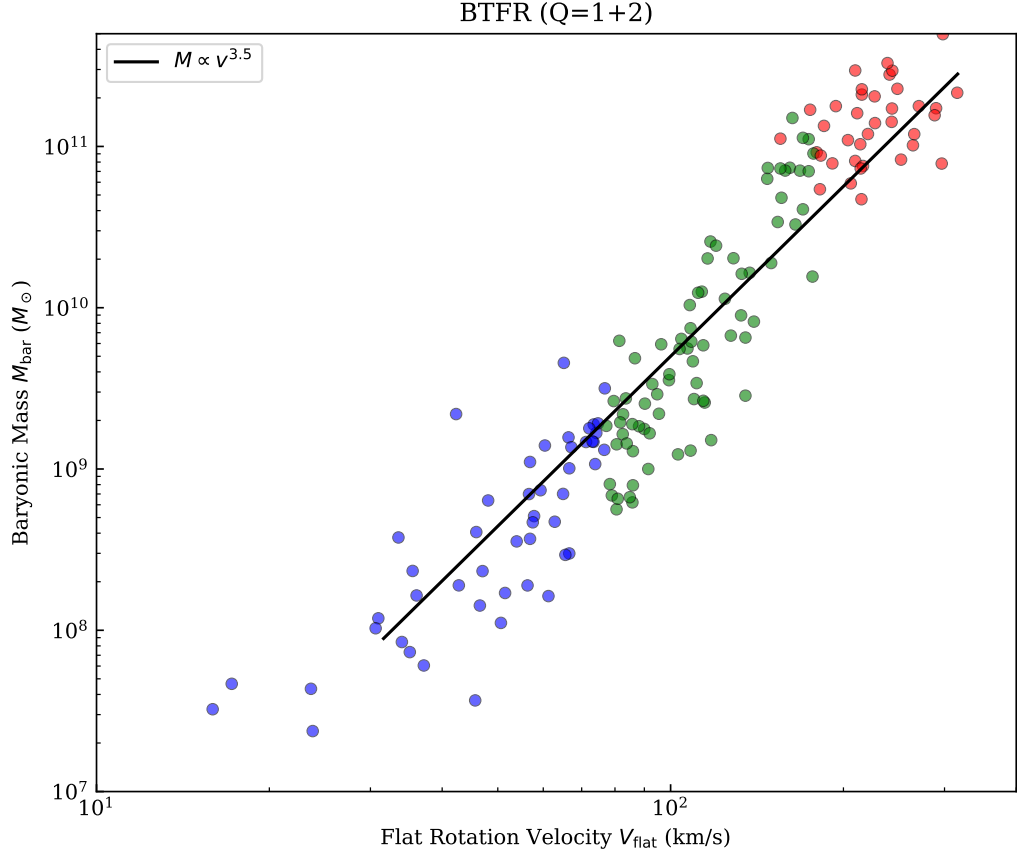


FIG. 16. Baryonic Tully-Fisher Relation for the combined Q=1 and Q=2 sample ( $N = 163$ ). The power-law scaling remains consistent with the Q=1 subset, with minimal additional scatter.

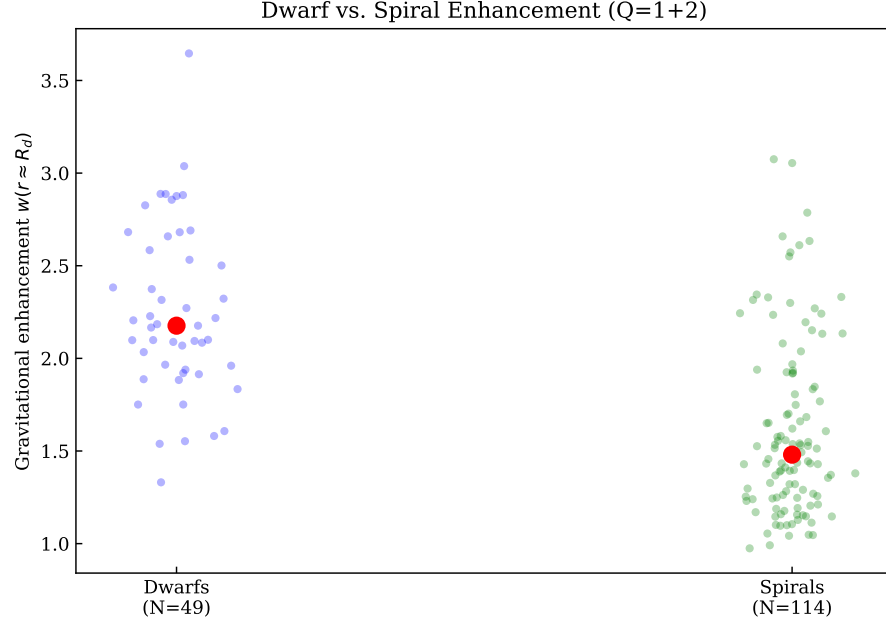


FIG. 17. Replication of the dwarf vs. spiral enhancement analysis using the extended  $Q=1$  and  $Q=2$  sample ( $N = 163$ ). The predicted enhancement ratio and distribution overlap remain consistent with the  $Q=1$  results, demonstrating that the morphological trend is robust to data quality variations.

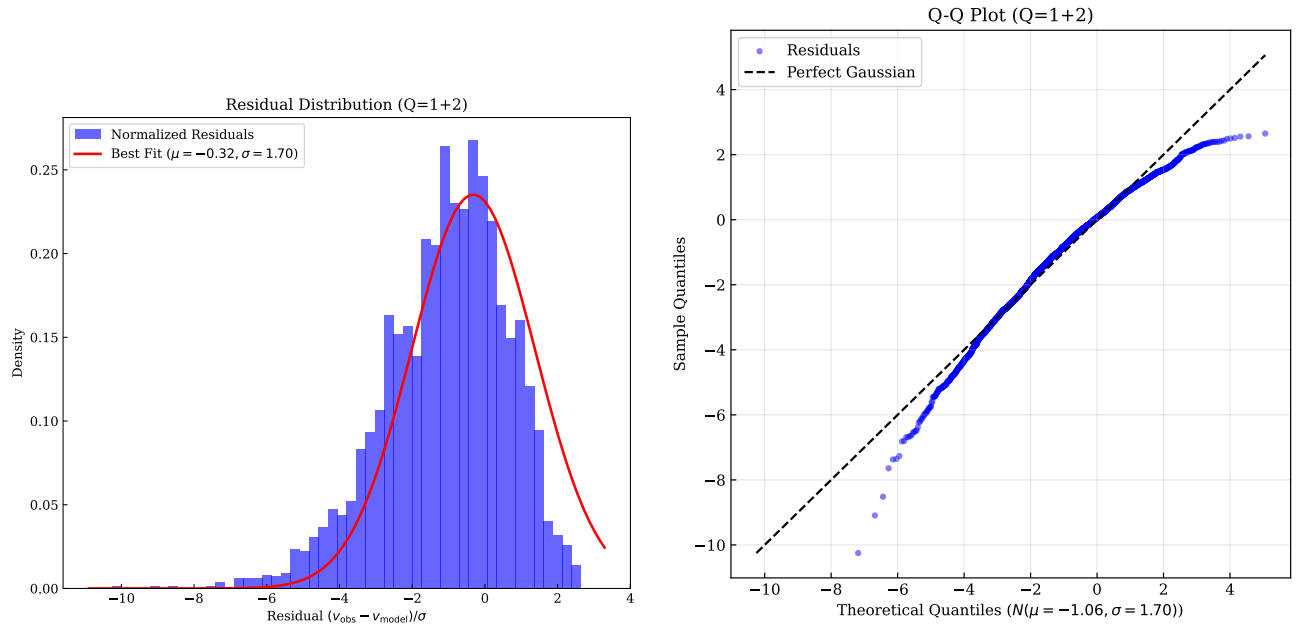


FIG. 18. Residual analysis extended to the combined  $Q=1+Q=2$  dataset. **Left:** Histogram with best-fit Gaussian. **Right:** Q-Q plot. The error distribution remains well-behaved and consistent with the  $Q=1$  results, showing no pathological deviations in the larger sample.

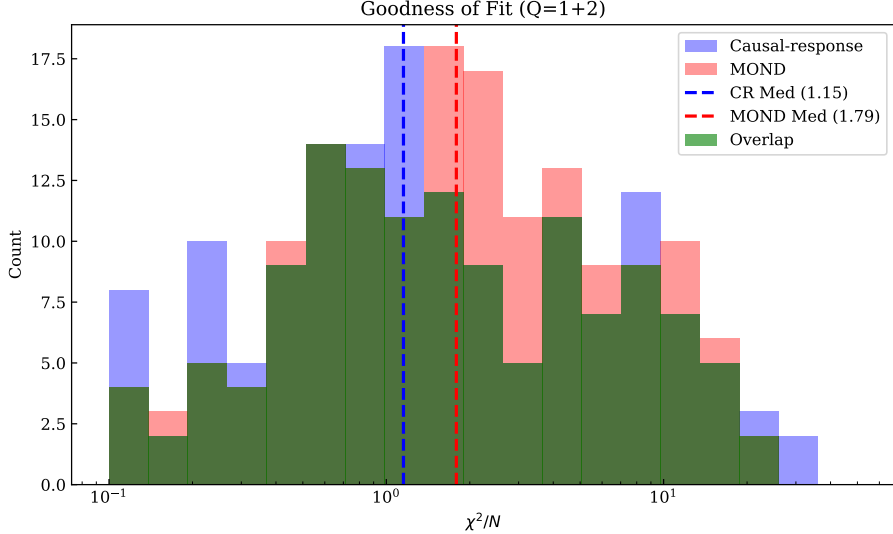


FIG. 19. Goodness-of-fit distribution for the combined  $Q=1+Q=2$  dataset ( $N = 163$ ). The median  $\chi^2/N$  improves slightly to 1.15, confirming that the model generalizes robustly to the larger sample.

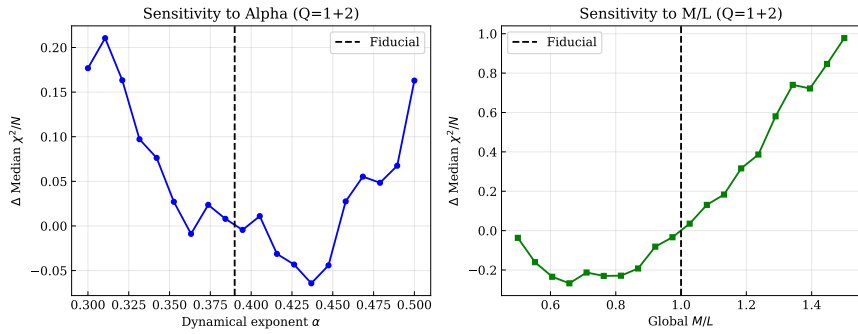


FIG. 20. Parameter sensitivity analysis repeated for the combined  $Q=1+Q=2$  dataset. The global minima for  $\alpha$  and  $M/L$  remain stable near the fiducial values ( $\alpha \approx 0.39$ ,  $M/L \approx 1.0$ ), indicating that the model's parameterization is robust against data quality variations.

- 
- [1] R. B. Tully and J. R. Fisher, *Astron. Astrophys.* **54**, 661 (1977).
- [2] S. S. McGaugh, J. M. Schombert, G. D. Bothun, and W. J. G. de Blok, *Astrophys. J. Lett.* **533**, L99 (2000).
- [3] S. S. McGaugh, *Astron. J.* **143**, 40 (2012).
- [4] V. C. Rubin and W. K. Ford, Jr., *Astrophys. J.* **159**, 379 (1970).
- [5] A. Bosma, *Astron. J.* **86**, 1825 (1981).
- [6] F. Zwicky, *Helv. Phys. Acta* **6**, 110 (1933).
- [7] D. Clowe *et al.*, *Astrophys. J. Lett.* **648**, L109 (2006).
- [8] Planck Collaboration, *Astron. Astrophys.* **641**, A6 (2020).
- [9] G. Bertone, D. Hooper, and J. Silk, *Phys. Rep.* **405**, 279 (2005).
- [10] J. F. Navarro, C. S. Frenk, and S. D. M. White, *Astrophys. J.* **490**, 493 (1997).
- [11] W. J. G. de Blok, *Adv. Astron.* **2010**, 789293 (2010).
- [12] S.-H. Oh *et al.*, *Astron. J.* **149**, 180 (2015).
- [13] A. Klypin, A. V. Kravtsov, O. Valenzuela, and F. Prada, *Astrophys. J.* **522**, 82 (1999).
- [14] B. Moore *et al.*, *Astrophys. J. Lett.* **524**, L19 (1999).
- [15] M. Boylan-Kolchin, J. S. Bullock, and M. Kaplinghat, *Mon. Not. R. Astron. Soc.* **415**, L40 (2011).
- [16] J. S. Bullock and M. Boylan-Kolchin, *Annu. Rev. Astron. Astrophys.* **55**, 343 (2017).
- [17] K. A. Oman *et al.*, *Mon. Not. R. Astron. Soc.* **452**, 3650 (2015).
- [18] S. S. McGaugh, F. Lelli, and J. M. Schombert, *Phys. Rev. Lett.* **117**, 201101 (2016).
- [19] E. Aprile *et al.* (XENON Collaboration), *Phys. Rev. Lett.* **121**, 111302 (2018).
- [20] M. Milgrom, *Astrophys. J.* **270**, 365 (1983).
- [21] B. Famaey and S. S. McGaugh, *Living Rev. Relativ.* **15**, 10 (2012).
- [22] R. H. Sanders and S. S. McGaugh, *Annu. Rev. Astron. Astrophys.* **40**, 263 (2002).
- [23] J. D. Bekenstein, *Phys. Rev. D* **70**, 083509 (2004).
- [24] T. P. Sotiriou and V. Faraoni, *Rev. Mod. Phys.* **82**, 451 (2010).
- [25] Y. Fujii and K. Maeda, *The Scalar-Tensor Theory of Gravitation* (Cambridge University Press, 2003).
- [26] C. de Rham, *Living Rev. Relativ.* **17**, 7 (2014).
- [27] E. Verlinde, *JHEP* **2011**, 29 (2011).
- [28] E. Verlinde, *SciPost Phys.* **2**, 016 (2017).
- [29] F. Lelli, S. S. McGaugh, and J. M. Schombert, *Astron. J.* **152**, 157 (2016).
- [30] S. S. McGaugh, F. Lelli, J. M. Schombert, P. Li, T. Visgaitis, K. S. Parker, and M. S. Pawlowski, *Astron. J.* **162**, 202 (2021). Available at [https://astroweb.case.edu/ssm/papers/McGaugh\\_2021\\_AJ\\_162\\_202.pdf](https://astroweb.case.edu/ssm/papers/McGaugh_2021_AJ_162_202.pdf).
- [31] A. O. Caldeira and A. J. Leggett, *Physica A* **121**, 587 (1983).
- [32] S. Deser and R. P. Woodard, *Phys. Rev. Lett.* **99**, 111301 (2007); see also *J. Phys. A* **46**, 214006 (2013).
- [33] T. Jacobson, *Phys. Rev. Lett.* **75**, 1260 (1995).
- [34] J. D. Bekenstein and M. Milgrom, *Astrophys. J.* **286**, 7 (1984).
- [35] M. Milgrom, *Mon. Not. R. Astron. Soc.* **403**, 886 (2010).
- [36] L. Berezhiani and J. Khouri, *Phys. Rev. D* **92**, 103510 (2015).
- [37] M. Van Raamsdonk, *Gen. Relativ. Gravit.* **42**, 2323 (2010).
- [38] G. 't Hooft, arXiv:gr-qc/9310026 (1993).
- [39] L. S. Susskind, *J. Math. Phys.* **36**, 6377 (1995).
- [40] K. G. Begeman, A. H. Broeils, and R. H. Sanders, *Mon. Not. R. Astron. Soc.* **249**, 523 (1991).
- [41] F. Fraternali *et al.*, *Astron. Astrophys.* **531**, A64 (2011).
- [42] M. A. W. Verheijen, *Astrophys. J.* **563**, 694 (2001).
- [43] F. Lelli *et al.*, *Mon. Not. R. Astron. Soc.* **468**, L68 (2017).
- [44] M. M. Brouwer *et al.*, *Mon. Not. R. Astron. Soc.* **466**, 2547 (2017).
- [45] S. W. Hawking, *Commun. Math. Phys.* **43**, 199 (1975).
- [46] J. M. Maldacena, *Adv. Theor. Math. Phys.* **2**, 231 (1998).
- [47] J. D. Bekenstein, *Phys. Rev. D* **7**, 2333 (1973).
- [48] S. Lloyd, *Phys. Rev. Lett.* **88**, 237901 (2002).
- [49] J. A. Wheeler, in *Complexity, Entropy, and the Physics of Information*, W. H. Zurek, ed. (Wesview Press, Boulder, CO, 1990).
- [50] C. E. Shannon, *Bell Syst. Tech. J.* **27**, 379 (1948).
- [51] A. S. Holevo, *Probl. Inf. Transm.* **9**, 177 (1973).
- [52] R. Landauer, *IBM J. Res. Dev.* **5**, 183 (1961).
- [53] N. Margolus and L. B. Levitin, *Physica D* **120**, 188 (1998).
- [54] M. G. Walker *et al.*, *Astrophys. J.* **704**, 1274 (2009).